



HAL
open science

ALMA observations of the η Corvi debris disc: inward scattering of CO-rich exocomets by a chain of 3–30 M_{\oplus} planets?

S. Marino, M. Wyatt, O. Panić, L. Matra, M. Kennedy, A. Bonsor, Q. Kral, W. Dent, G. Duchene, D. Wilner, et al.

► To cite this version:

S. Marino, M. Wyatt, O. Panić, L. Matra, M. Kennedy, et al.. ALMA observations of the η Corvi debris disc: inward scattering of CO-rich exocomets by a chain of 3–30 M_{\oplus} planets?. Monthly Notices of the Royal Astronomical Society, 2016, 465 (3), pp.2595-2615. <10.1093/mnras/stw2867>. <hal-02231923>

HAL Id: hal-02231923

<https://hal.science/hal-02231923v1>

Submitted on 28 Jan 2022

HAL is a multi-disciplinary open access archive for the deposit and dissemination of scientific research documents, whether they are published or not. The documents may come from teaching and research institutions in France or abroad, or from public or private research centers.

L'archive ouverte pluridisciplinaire **HAL**, est destinée au dépôt et à la diffusion de documents scientifiques de niveau recherche, publiés ou non, émanant des établissements d'enseignement et de recherche français ou étrangers, des laboratoires publics ou privés.



Distributed under a Creative Commons CC BY 4.0 - Attribution - International License

ALMA observations of the η Corvi debris disc: inward scattering of CO-rich exocomets by a chain of 3–30 M_{\oplus} planets?

S. Marino,^{1*} M. C. Wyatt,¹ O. Panić,^{1,2†} L. Matrà,¹ G. M. Kennedy,¹ A. Bonsor,¹ Q. Kral,¹ W. R. F Dent,³ G. Duchene,^{4,5} D. Wilner,⁶ C. M. Lisse,⁷ J.-F. Lestrade⁸ and B. Matthews⁹

¹*Institute of Astronomy, University of Cambridge, Madingley Road, Cambridge CB3 0HA, UK*

²*School of Physics and Astronomy, University of Leeds, Woodhouse Lane, Leeds LS2 9JT, UK*

³*Joint ALMA Observatory, Alonso de Córdova 3107, 763-0355 Vitacura, Santiago, Chile*

⁴*Department of Astronomy, UC Berkeley, Berkeley, CA 94720, USA*

⁵*Univ. Grenoble Alpes/CNRS, IPAG, F-38000 Grenoble, France*

⁶*Harvard–Smithsonian Center for Astrophysics, 60 Garden Street, MS-78, Cambridge, MA 02138, USA*

⁷*Space Exploration Sector, Johns Hopkins University Applied Physics Laboratory, 11100 Johns Hopkins Road, Laurel, MD 20723, USA*

⁸*Observatoire de Paris - LERMA, CNRS, 61 Av. de l’Observatoire, F-75014 Paris, France*

⁹*National Research Council of Canada Herzberg Astronomy and Astrophysics Programs, 5071 West Saanich Road, Victoria, BC, V9E 2E7, Canada*

Accepted 2016 November 3. Received 2016 November 2; in original form 2016 October 3

ABSTRACT

While most of the known debris discs present cold dust at tens of astronomical unit (au), a few young systems exhibit hot dust analogous to the Zodiacal dust. η Corvi is particularly interesting as it is old and it has both, with its hot dust significantly exceeding the maximum luminosity of an *in situ* collisional cascade. Previous work suggested that this system could be undergoing an event similar to the Late Heavy Bombardment (LHB) soon after or during a dynamical instability. Here, we present ALMA observations of η Corvi with a resolution of 1.2 arcsec (~ 22 au) to study its outer belt. The continuum emission is consistent with an axisymmetric belt, with a mean radius of 152 au and radial full width at half-maximum of 46 au, which is too narrow compared to models of inward scattering of an LHB-like scenario. Instead, the hot dust could be explained as material passed inwards in a rather stable planetary configuration. We also report a 4σ detection of CO at ~ 20 au. CO could be released *in situ* from icy planetesimals being passed in when crossing the H₂O or CO₂ ice lines. Finally, we place constraints on hidden planets in the disc. If a planet is sculpting the disc’s inner edge, this should be orbiting at 75–100 au, with a mass of 3–30 M_{\oplus} and an eccentricity < 0.08 . Such a planet would be able to clear its chaotic zone on a time-scale shorter than the age of the system and scatter material inwards from the outer belt to the inner regions, thus feeding the hot dust.

Key words: circumstellar matter – stars: individual: HD 109085 – planetary systems – radio continuum: planetary systems.

1 INTRODUCTION

As a byproduct of planet formation, discs of kilometre-sized bodies or planetesimals can form, analogous to the Asteroid and Kuiper belts in the Solar system (Lissauer 1993). Destructive collisions between these bodies can give rise to debris discs, grinding down the largest bodies producing a wide size distribution of solids,

from micrometre-sized dust grains up to the size of asteroids or comets, in a so-called collisional cascade (Wyatt et al. 2007b). This has been proven observationally using multiwavelength observations (see Backman & Paresce 1993). Moreover, the last decade of debris disc surveys has shown that Kuiper belt analogues are quite common, with detection rates of at least 20 per cent around AFGK stars (Su et al. 2006; Hillenbrand et al. 2008; Carpenter et al. 2009; Eiroa et al. 2013; Thureau et al. 2014; Matthews et al. 2014). These surveys have also shown that the levels of infrared excess decay with stellar age, as expected from collisional models.

* E-mail: sebastian.marino.estay@gmail.com

† Royal Society Dorothy Hodgkin Fellow.

By studying the spectral energy distribution (SED) of systems with detected dust, it is possible to estimate the temperature and radial location of the dust assuming standard optical properties (e.g. Kennedy & Wyatt 2014). While in most of the known debris discs the dust grains are located in narrow belts at tens of astronomical unit (au), analogous to the Kuiper belt, a small fraction of discs have been identified to host a hot dust component within a few au, analogous to the Asteroid belt or Zodiacal dust (e.g. Absil et al. 2013). The majority of these discs with hot dust are younger than ~ 100 Myr old (Kennedy & Wyatt 2013), e.g. HD 172555 (Lisse et al. 2009).

Since collisional time-scales are a steep function of the distance to the star (Löhne, Krivov & Rodmann 2008), debris discs at a few au are expected to evolve much faster than Kuiper belt analogues. This implies that there is a maximum possible disc mass at a given radius and age, and thus a maximum dust luminosity (Wyatt et al. 2007b; Löhne et al. 2008). However, an important subset of discs with hot dust around old ($\gg 100$ Myr) stars exceeds this limit by 3 orders of magnitude or more, precluding its explanation as a result of destructive collisions between planetesimals *in situ* (Wyatt et al. 2007a). Therefore, in most of these systems the planetesimals feeding the hot dust component must be located farther from the star, in a cold belt of planetesimals where collisions are less frequent and the disc mass decays more slowly.

Among the sample of old stars with hot dust, the 1–2 Gyr old F2V star η Corvi (HD 109085, HIP 61174, Ibukiyama & Arimoto 2002; Mallik, Parthasarathy & Pati 2003; Vican 2012, hereafter assumed to be 1.4 Gyr old, consistent with isochrone fitting in the HR diagram), located 18.3 pc away (van Leeuwen 2007), is particularly interesting because it presents both a hot and a cold dust component in its SED, where the hot dust exceeds the brightness limit mentioned above. Its infrared excess was first detected with *IRAS* (Stencel & Backman 1991), after which several observations from the optical to the millimetre have targeted this system. From mid-infrared observations, Smith, Wyatt & Haniff (2009) determined that the hot dust must be located within 3 au from the star. More recent observations with the Large Binocular Telescope Interferometer (LBTI) and the Keck Interferometer have confirmed this and determined that the hot component is located at projected separations of ~ 1.4 au and 0.2–0.8 au from the star, respectively (Defrère et al. 2015; Kennedy et al. 2015; Lebreton et al. 2016). Moreover, we know that the hot dust luminosity has stayed almost constant over the last three decades (Duchêne et al. 2014). On the other hand, Wyatt et al. (2005) resolved the cold component of the system with SCUBA/JCMT at millimetre wavelengths, finding that it has a mean radius of ~ 150 au. At 70 μm *Herschel* imaged both hot and cold components, resolving the outer belt and confirming that the hot dust has large amounts of small dust below the blow-out size (previously known from *IRS*; Chen et al. 2006) providing further evidence that the hot dust cannot be explained by a steady-state collisional cascade and suggesting a more violent origin (Duchêne et al. 2014).

Several scenarios have been proposed to explain the high levels of mid-infrared emission in η Corvi. Wyatt et al. (2010) suggested that the system could host a population of highly eccentric planetesimals, colliding at pericentre within a few au producing the hot dust and observed excess. These planetesimals would survive for longer time-scales due to their large apocentre in the cold belt. While this scenario is appealing in connecting the inner and outer dust components in the system, it was ruled out by *Herschel* resolved observations (Duchêne et al. 2014) as no emission is detected between the hot dust location and the outer belt. The hot dust could be also a product of a giant impact on a planet close in or recent giant

collision in an *in situ* Asteroid belt rather than an ongoing collisional cascade. This would be consistent with the spectroscopic features of impact produced silica and high-temperature carbonaceous phases revealed by *Spitzer* (Chen et al. 2006; Lisse et al. 2012). While these events are expected to be rare and the produced small dust short lived compared to the age of the system (Kral et al. 2015), η Corvi is one of just two FGK stars with hot dust at this level out of the DEBRIS sample of ~ 300 stars, i.e. we cannot exclude an unlikely scenario as we could be witnessing the system at a special time. However, the hot dust also displays spectral features of primitive cometary material consistent with icy solids formed further out in the system (Lisse et al. 2012), and thus, transported by an unknown process to within a few au. There are two known mechanisms that can transport material inwards, Poynting–Robertson (PR) drag and interactions with single or multiple planets. The first can deliver small grains from the outer disc to the inner regions, but this mechanism is not efficient enough to explain the hot dust in η Corvi, given the low optical depth or fractional luminosity of the outer belt (Kennedy & Piette 2015). Thus, it seems necessary to invoke the presence of planets in the system.

Therefore, three scenarios remain that could explain the hot dust level and its composition: (1) the system is going through an instability, analogous to the Late Heavy Bombardment (LHB) in the Solar system, scattering comets from the outer belt to the innermost regions (e.g. Bonsor, Raymond & Augereau 2013); (2) planets in a rather stable configuration in the system are scattering dust from the outer disc feeding the hot dust or bigger icy solids that then collide closer in producing the hot dust (e.g. Bonsor, Augereau & Thébault 2012); (3) planetesimals are scattered by planets in the system, colliding with a planet within a few au releasing large amounts of debris. Thus, we are interested in studying the structure of the outer belt to look for features that can hint at one of the three possible planet-driven scenarios described above to explain the hot dust.

In this paper, we present the first continuum observations of η Corvi with the Atacama Large Millimeter/submillimeter Array (ALMA) to study in detail the continuum dust emission of its cold outer belt at 0.88 mm. At this wavelength, the continuum is dominated by millimetre-sized dust grains (~ 0.1 – 10.0 mm), for which radiation forces are negligible. Thus, they trace the distribution of the parent planetesimals which contain the bulk of the disc mass and may provide clues to the mechanism feeding the hot dust closer in. In Section 2, we describe the ALMA observations, continuum imaging and search for any CO emission in the disc. Then, in Section 3 we model the continuum data with parametric disc models to study the distribution of planetesimals in the disc. We also derive CO gas masses and upper limits considering non-LTE. In Section 4, we discuss the implications of the ALMA continuum data, how it fits with the hypothesis of material being transported from the outer to the inner regions of the disc; we also discuss the origin of the tentative CO gas detection, and we place some constraints on a planet between the hot dust and outer belt based on the continuum observations. Finally, in Section 5 we summarize the main results and conclusions of our work.

2 OBSERVATIONS

ALMA band 7 observations (340 GHz) of η Corvi were carried out from 2013 Dec 15 to 2015 Jan 1 under the project 2012.1.00385.S (PI: M. C. Wyatt), resulting in six successful executions. Each set of observations is a three-point mosaic along the disc major

Table 1. Summary of science observations.

Date of observations	Elevation [deg]	n_{ant}	t_{sci} [min]	Per cent flagged	Image rms [μJy]	Flux calibrator	Bandpass calibrator	Phase calibrator
2013 Dec 15	51–61	27	40	16	90	Pallas	J1058–0133	J1215–1731
2013 Dec 15	70–79	27	40	40	90	Ceres	J1256–0547	J1215–1731
2014 Dec 25	72–83	38	48	20	60	3c279	J1256–0547	J1245–1616
2014 Dec 26	77–83	40	48	18	40	Ganymede	J1256–0547	J1245–1616
2014 Dec 29	66–81	37	48	15	50	Titan	J1256–0547	J1245–1616
2015 Jan 01	62–77	37	48	20	50	Titan	J1256–0547	J1245–1616

axis, separated by 8.8 arcsec and centred on η Corvi. The primary beam full width at half-maximum (FWHM) of a single pointing is 17.9 arcsec, which allowed us to reach a combined primary beam efficiency above 50 per cent in an elongated region of 36×18 arcsec² oriented as the disc in the sky. Array configurations were very compact, with baselines ranging from 15 to 445 m, with the 5th and 95th percentiles equal to 26 and 240 m. This allows to recover angular scales from 1 arcsec to 7 arcsec.

The band 7 spectral setup consisted of four spectral windows. Three were set to observe the continuum emission centred at 335.744, 337.644 and 347.455 GHz, each one with 128 channels of 14 km s⁻¹ width (effective spectral resolution of 28 km s⁻¹), obtaining a 2 GHz total bandwidth per spectral window. The fourth included the ¹²CO 3–2 line at 345.798 GHz and was set with 3840 finer channels, each one with a width of 0.42 km s⁻¹ (effective spectral resolution of 0.82 km s⁻¹), obtaining a total bandwidth of 1.9 GHz. The four together provided an effective bandwidth of 7.9 GHz to study the continuum emission.

Table 1 provides a summary of the six sets of science observations of η Corvi spanning approximately one year as the ALMA array expanded from $n_{\text{ant}} \approx 30$ to ≈ 40 antennas. Consequently, the most sensitive observations were the ones obtained most recently. We can also see that the science target has always been observed at a relatively high elevation. The total time on-source t_{sci} shown corresponds to the sum of the three pointings in the mosaic, so the actual time spent on-source with the pointing on the location of η Corvi itself is one third of t_{sci} . Pallas, Ceres, 3c279, Ganymede and Titan were used as flux calibrators and observed for 2.6 min; J1058–0133 and J1256–0547 as bandpass calibrators and observed for 5.3 min; and J1215–1731 and J1245–1616 as phase calibrators and observed for 10.9 and 14.1 min in total on each science observation, respectively.

η Corvi has a significant proper motion of -425.2 ± 0.2 and -57.2 ± 0.1 mas yr⁻¹ in RA and Dec. direction, respectively (van Leeuwen 2007), and consequently the pointing of the mosaic had to be adjusted for each observation. Unfortunately, due to an identified and subsequently corrected error in carrying out mosaic observations¹ the pointings were not always consistently centred on the star and neither were the offsets always equal. These errors were corrected using the CASA task fixvis (McMullin et al. 2007) and subsequently aligning and combining the data prior to the image synthesis. Deviations of up to +0.36 arcsec in RA and +0.48 arcsec in Dec. were made. This is sufficiently small compared to the FWHM of the primary beam to allow to successfully combine the observations, achieving the desired rms.

¹ Described in <https://almascience.eso.org/news/notification-of-problem-affecting-certain-alma-data-that-used-mosaic-and-offset-pointing-observing-modes>

2.1 Continuum emission

The image reconstruction of the dust continuum is performed with the CLEAN algorithm and task in CASA 4.4 (McMullin et al. 2007), using natural weights, and combining the four spectral windows to recover the highest signal-to-noise ratio (S/N). As the dirty image of the data has strong negative artefacts between the stellar emission and the outer belt, we first clean the stellar emission and then the outer belt. Using natural weights, we obtain an elongated beam of size 1.18×0.65 arcsec² (equivalent to 22×12 au), with its major axis oriented with a position angle (PA) of 89°. The image noise level before correcting by the primary beam is 20 $\mu\text{Jy beam}^{-1}$ (which does not take into account the uncertainty on the absolute flux calibration, ~ 10 per cent). This is estimated measuring the image standard deviation in an elliptic annulus far from the disc emission. Finally, we corrected by the primary beam obtaining an image noise that increases with distance to the star as the primary beam efficiency decreases. The image noise around the outer belt varies from 22 $\mu\text{Jy beam}^{-1}$ near the disc major axis up to 30 $\mu\text{Jy beam}^{-1}$ close to the minor axis. In Fig. 1, we present the CLEAN image tapering the visibilities with the Fourier transform of a Gaussian of FWHM of 1.2 arcsec, to obtain a less elongated beam of 1.5×1.3 arcsec² with a PA of 88°, and higher S/N per beam. At the centre of the tapered image, the noise level is 30 $\mu\text{Jy beam}^{-1}$, varying from 33 to 45 $\mu\text{Jy beam}^{-1}$ around the outer belt. Substructure is present along the belt in the CLEAN image, with two minima to the south west of the star. However, the emission is still consistent with an axisymmetric belt given the S/N (see Section 3). Compared with the PACS image at 70 μm obtained by *Herschel* (previous best image of the outer belt), we obtain a spatial resolution four times higher or a 50 per cent higher S/N if we degrade the ALMA image to the PACS resolution.

Using the non-tapered image, we obtain an intensity peak of 258 ± 20 $\mu\text{Jy beam}^{-1}$ at the stellar location, which is consistent with the expected photospheric emission of 250 ± 7 μJy , extrapolated from the available photometry at 2.2, 3.6, 3.8, and 4.8 μm assuming a spectral index of 2 (Sylvester et al. 1996). However, the stellar emission at these wavelengths could deviate significantly from Rayleigh–Jeans as observed for the Sun (e.g. Loukitcheva et al. 2004; Fontenla, Balasubramaniam & Harder 2007). Subtracting the extrapolated stellar flux we can place an upper limit on any extra emission, e.g. hot dust. Considering the different uncertainties we find a 3σ upper limit of 100 μJy on the hot dust flux at 0.88 mm, higher than the 44 μJy extrapolated from the 70 μm flux excess detected with *Herschel* (Duchêne et al. 2014) using a spectral index of 2.0 (optimistic prediction), and far above the 1.5 μJy predicted by the hot dust model presented in the same study to fit the SED. Therefore, it is not surprising that no hot dust emission is detected.

We measure a total disc flux of 9.2 ± 0.5 mJy, integrating the continuum emission inside an elliptic mask with the same orientation and ellipticity as the disc, i.e. inclination (i) of 35° and a PA of 117° (the estimation of i and PA is presented in Section 3, obtaining

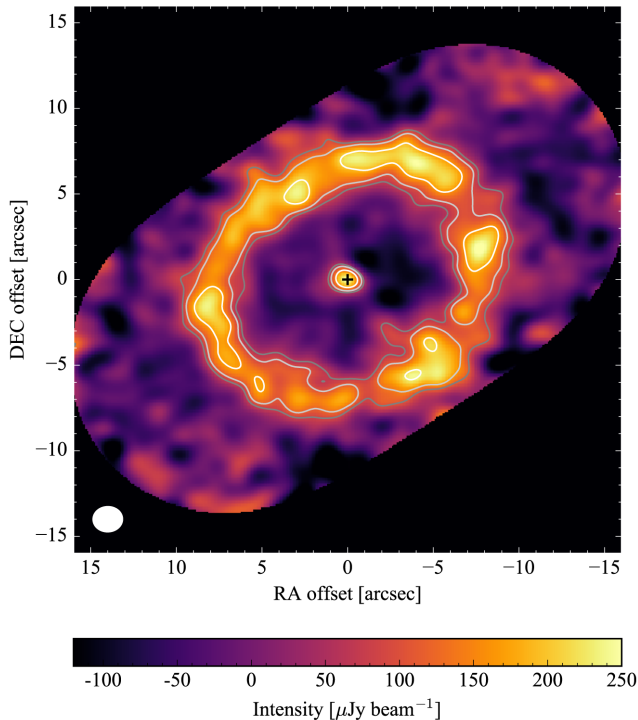


Figure 1. ALMA dust continuum CLEAN image at 0.88 mm (Band 7), with natural weights, primary beam corrected, and tapered by a Gaussian of FWHM of 1.2 arcsec. The beam size is 1.5×1.3 arcsec² and is represented by a white ellipse in the bottom left corner. At the centre of the image, the noise level is $30 \mu\text{Jy beam}^{-1}$. The black masked region indicates a primary beam response below 40 per cent. The contours represent emission above two, three and five times the local noise level. The x - and y -axes indicate the offset from the stellar position in R.A. and Decl. in arcsec, i.e. north is up and east is left. The stellar position is marked with a black ‘+’.

values consistent with previous *Herschel* observations; Lebreton et al. 2016), and with semimajor axis of 11 arcsec. However, we notice that there is significant negative emission inside the outer belt. These negatives may occur when deconvolving visibility data using the CLEAN image reconstruction algorithm, which does not impose positivity. If we integrate the flux inside an elliptic annulus of minimum and maximum semimajor axes 6 and 11 arcsec, we obtain a higher integrated flux of 10.1 ± 0.4 mJy, where the uncertainties stated above only consider the image noise.

At a similar wavelength of 0.85 mm, SCUBA-2/JCMT observed η Corvi measuring a total flux of 15.5 ± 1.4 mJy. Extrapolating this to 0.88 mm with a spectral index of 3.0, i.e. 14.0 ± 1.3 mJy, we find that the total emission measured in the ALMA CLEAN image is lower by $2\text{--}3\sigma$ considering absolute flux calibration uncertainties. The difference could be due to extended emission missed by an insufficient number of short baselines or due to the image reconstruction method. In Section 3, we model the disc emission by fitting different disc models to the visibilities, and thus we obtain disc fluxes that do not rely on the image deconvolution method. Fitting a simple axisymmetric belt, we find a total flux of 13.3 ± 1.6 , consistent with the total flux measured by SCUBA-2/JCMT at a similar wavelength.

As mentioned above, we find some non-negligible artefacts in the reconstructed images of the data. These appear both in the dirty and CLEAN images. These could be caused by (1) extended emission not captured by the uv -coverage due to insufficient short baselines; (2) the gridding of the visibilities when computing the fast Fourier trans-

form, which can produce a dirty image that does not approximate well to the true sky brightness for our uv -coverage; (3) imprecisions in the uv coordinates due to pointing errors when carrying out the mosaic observations as mentioned before. Because the negatives appear both at the real and at simulated observations (see Section 3), as well as using a different gridding or a uv -sampling when simulating observations, it is unlikely that the negatives are caused by (2) and (3). This shows the importance of having a complete uv -coverage that includes baselines that can capture the angular size of the observed source, e.g. including the 7-m array (the Atacama Compact Array) in ALMA observations or combining with the submillimeter array (SMA) observations. Moreover, in such cases of incomplete uv -sampling, e.g. insufficient number of short baselines, models should be compared with interferometric observations in the visibility space as reconstructed images can suffer from non-negligible artefacts.

To study the radial profile of the surface brightness we compute the average intensity over 40° wide wedges along the major and minor axes, and the average intensity profile at all azimuths around ellipses oriented as above. Each point in the intensity profiles corresponds to the mean intensity over 100 points equidistant in PA around an ellipse with a fixed semimajor axis or distance. The intensity at each point around the ellipses is calculated based on the value of the nearest pixel of the non-tapered CLEAN image. This is analogous to using elliptic annuli with radial widths of 0.1 arcsec (pixel size of the deconvolved image). Finally, the uncertainty of the radial profile is calculated as the squared root of the mean squared rms along each ellipse, divided by the square root of the number of independent points around the ellipse, approximated as the perimeter of the ellipse divided by the beam major axis. Fig. 2 shows the intensity profiles. We stress that points in the radial profile separated by less than ~ 1 arcsec (beam size) are not independent. The peak intensity along the major and minor axes is $70 \pm 8 \mu\text{Jy beam}^{-1}$ and $81 \pm 12 \mu\text{Jy beam}^{-1}$, respectively, both consistent within the uncertainties, while the average profile at all azimuths has a peak intensity of $79 \pm 4 \mu\text{Jy beam}^{-1}$. Along the major axis of the disc, the belt peaks at 8.30 ± 0.05 arcsec² (151 ± 1 au), where the error is estimated as $\sim \text{Beam}_{\text{fwhm}}/(S/N)$, with $S/N \sim 26$ at the peak – this uncertainty could be underestimated as the relation above is strictly valid only for point sources. The deprojected radial profile in the lower panel of Fig. 2 shows that the belt is clearly spatially resolved, spanning over ~ 4 arcsec, or ~ 70 au in radial extent.

Similarly, we study the surface brightness variations along PA averaging the disc emission radially between 120 and 180 au, and over arcs of 18° . This is shown in Fig. 3. Unlike Duchêne et al. (2014) where they found evidence of asymmetric disc emission at $70 \mu\text{m}$ with the north-west side having a peak intensity higher by a factor of 1.4 compared to the south-east side (see their fig. 5), we find no evidence of such asymmetries around the azimuthal profile of the belt. In fact, following the same procedure as they did, we compare the peak intensity of the averaged radial profile of the north-west with the south-east ansae, finding that they are consistent within uncertainties (ratio of 0.8 ± 0.1 with the south-east being brighter) and the first cannot be brighter by more than a factor of 1.2 (3σ limit). However, if we study the contribution to the total flux from the north-west and south-east halves of the disc (divided by the minor axis of the disc), we find that they have fluxes of 5.6 ± 0.3 and 4.5 ± 0.3 mJy, respectively. This is marginal evidence for emission excess on the north-west side of the disc as the *Herschel* showed, but still consistent with being axisymmetric.

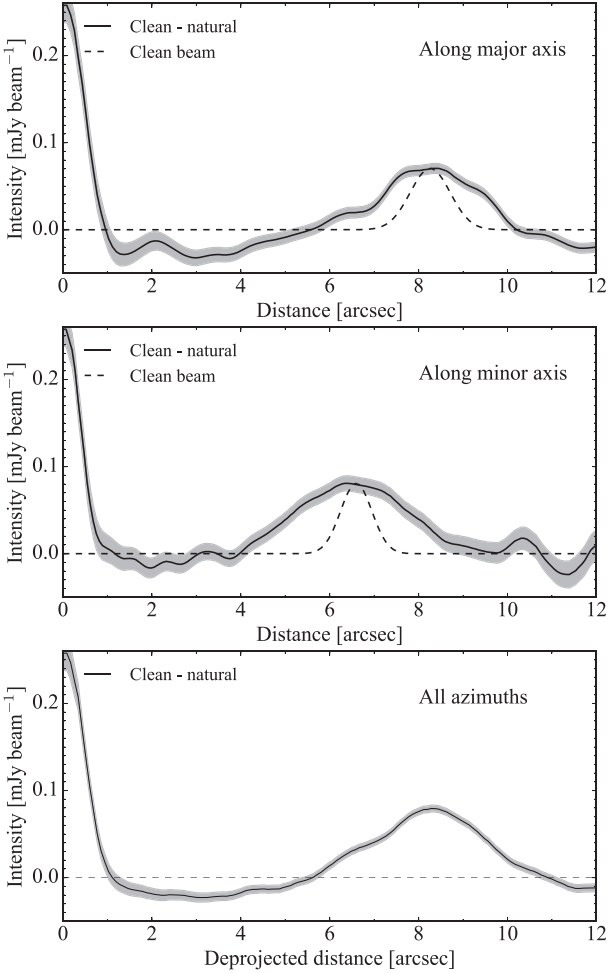


Figure 2. Intensity radial profiles of the dust continuum versus distance to the star along the major (top panel) and minor axes of the disc (middle panel) obtained averaging over 40° wide wedges. In the bottom panel, we present the mean intensity at all azimuths versus the deprojected distance to the star. The grey areas represent the 68 per cent confidence region.

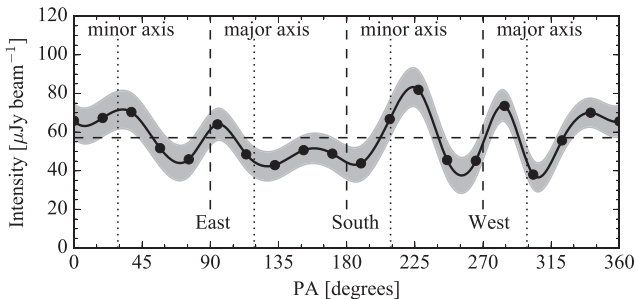


Figure 3. Intensity azimuthal profiles of the dust continuum emission versus PA obtained averaging over elliptic annuli of semimajor axes between 6.8 and 9.8 arcsec (equivalent to 125 and 180 au) and over 18° wide wedges (centred at the black dots). The continuous line is obtained with a cubic spline interpolation between the black dots. The horizontal-dashed line represents the mean intensity around the outer belt. The grey area represents the 68 per cent confidence region.

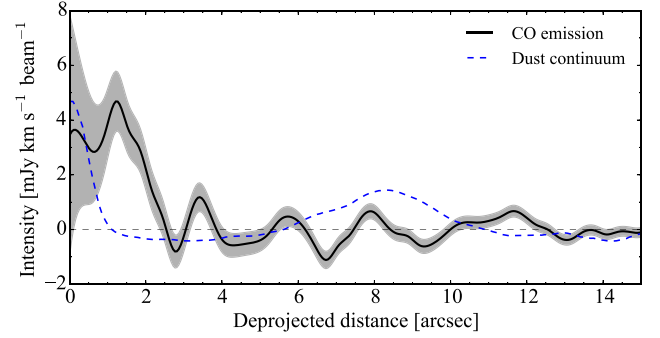


Figure 4. Mean CO intensity versus distance to the star obtained by azimuthally averaging the continuum-subtracted dirty channel maps and integrating over the line width expected due to Keplerian rotation, assuming a heliocentric stellar RV of 1.5 km s^{-1} . The grey areas represent the 68 per cent confidence region.

2.2 CO (3–2)

The increasing number of gas detections in young debris discs has opened a debate over whether primordial gas can remain in the disc for more than 10 Myr, or whether it can be of secondary origin, e.g. being released by volatile-rich icy solids in the disc. After subtracting the continuum emission from the visibilities using the CASA task *uvcontsub*, we search for any CO $J = 3 - 2$ gas emission that could be present in the system. We find no significant CO gas emission along the continuum-subtracted dirty channel maps (CLEAN is not necessary as there is no significant emission in the dirty channel maps). As shown by Matrà et al. (2015) and Marino et al. (2016), the detection limits can be improved by azimuthally averaging the dirty channel maps and integrating in frequency. Similar to the method presented in the previous section, we calculate the mean CO intensity at different radii azimuthally averaging the continuum-subtracted dirty channel maps around ellipses oriented as the outer belt (see Section 3.1). We also integrate the emission in frequency or radial velocity (RV) between the minimum and maximum RV expected from Keplerian rotation at each radii, and assuming the same inclination as the outer belt (37°). We restrict the maximum RV to 6 km s^{-1} , equivalent to the maximum RV at 10 au from the star as we cannot spatially resolve emission within 10 au. The stellar RV, v_* , is not very well constrained in this system with measurements ranging between -2.8 and 1.8 km s^{-1} in the heliocentric reference frame (Gontcharov 2006; Casagrande et al. 2011). Therefore, we vary v_* between -10 and 10 km s^{-1} to search for any significant CO disc emission that could be present in the data. At each radius we estimate the uncertainty based on the rms on each channel, the number of independent spectral resolution elements considered ($\sim \frac{\text{number of channels}}{2.667}$, due to Hanning smoothing²) and the number of independent beams around each ellipse ($\sim \frac{\text{perimeter of ellipse}}{\text{beam major axis}}$).

In Fig. 4, we present the mean intensity profile spectrally integrated assuming $v_* = 1.5 \text{ km s}^{-1}$. The continuum radial profile is overlaid in blue-dashed line. We find an intensity peak of $4.7 \pm 1.1 \text{ mJy beam}^{-1} \text{ km s}^{-1}$ at ~ 1.2 arcsec. This peak is present above 3σ for v_* ranging from -0.5 to 5.0 km s^{-1} . Apart from the peak at ~ 1.2 arcsec from the star, no significant emission is detected. The peak of the emission corresponds to a radius of 22 ± 6 au, where the uncertainty is estimated as the beam semimajor axis divided

² https://safe.nrao.edu/wiki/pub/Main/ALMAWindowFunctions/Note_on_Spectral_Response.pdf

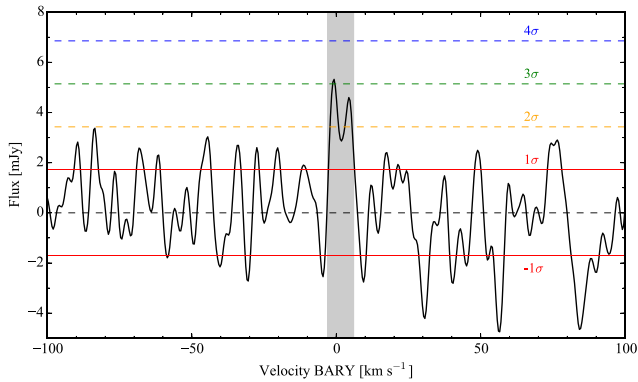


Figure 5. Continuum-subtracted integrated spectrum inside an elliptic mask of minimum and maximum semimajor axes of 0.8 and 2.0 arcsec, and oriented as the dust continuum outer belt. The original spectrum was smoothed with a Gaussian kernel with standard deviation of 2.5 channels. The horizontal lines represent ± 1 , 2, 3 and 4σ levels. The grey region represents velocities between -2.7 and 6.3 km s^{-1} , equivalent to the line width expected due to Keplerian rotation at ~ 20 au (1 arcsec). The velocities represent the Doppler shift with respect to 345.796 GHz in the barycentric reference frame.

by the S/N. This implies that the putative detection is not strictly co-located with the hot dust. Note that the sensitivity of the intensity profile varies with radius because the number of beams and spectral resolution elements over which we are integrating changes with radius. Therefore, it is possible that similar or even higher CO levels are present within 1.2 arcsec, where the integrated sensitivity is lower.

In Fig. 5, we present a spectrum obtained by integrating the dirty map over an elliptic mask oriented as the outer belt and with an inner and outer semimajor axes of 0.8 arcsec to 2.0 arcsec (15 to 37 au), respectively, to maximize the S/N. We also smoothed the spectrum convolving it with a Gaussian kernel with a standard deviation of 2.5 channels or 1.1 km s^{-1} . The spectrum shows a double peaked line centred at 1.8, consistent with the expected profile for a ring of CO gas rotating around the star at a radius of ~ 20 au. The total line flux between -2.7 km s^{-1} and 6.3 km s^{-1} is 38 ± 9 mJy km s^{-1} (4σ). This is used in Section 3.7 to estimate the mass of CO that could be present at this location. If the gas is in Keplerian rotation, the emission should have a butterfly pattern, with half of the emission having a positive or negative Doppler shift and arise from either the south-east or north-west half of the disc (separated by the minor axis of the disc). Thus, we try to integrate the emission on one half of the disc for positive Doppler shifts and on the other half for negative Doppler shifts to reduce the integrated noise. We find similar S/N for both possible disc orientations, slightly preferring the north-western and south-eastern halves having positive and negative Doppler shifts, respectively, but not at a significant level. With the preferred orientation we obtain a S/N of 3.9 for the integrated flux, while with the opposite the S/N is 3.4. The small difference in S/N shows that there is emission with the same Doppler shift on both halves of the disc, in contradiction with the Keplerian and disc orientation assumption. This could be due to the emission being not very well constrained in position as we are using the dirty channel maps, the uncertain stellar RV, the disc orientation being different compared to the outer belt, or deviations from Keplerian rotation. We can also estimate the likelihood of that any search of CO conducted over the range $v_* = \pm 10$ km s^{-1} and over annuli with semimajor axes within the range 0–8 arcsec would result in a 4σ detection. We find that this has a probability

of 1 per cent. The origin of this emission if real is discussed in Section 4.2. Deeper ALMA observations are necessary to confirm this detection and study the gas rotation pattern.

In order to place upper limits on the total CO emission from the outer belt and inner component (co-located with the hot dust), we compute the uncertainty on the total flux given the noise level on each channel map and the number of velocity channels to consider. Around the outer belt we obtained an integrated noise level of 12 mJy km s^{-1} integrating azimuthally and radially along the belt seen in continuum emission (from 130 to 170 au), and in velocity at the expected RV on each pixel due to Keplerian rotation and 37° inclination. For the inner component, we integrate the emission inside 1.2 arcsec between ± 21 km s^{-1} (expected line width assuming no emission is coming from a radii smaller than 1 au) obtaining an integrated noise level of 11 mJy km s^{-1} . Based on this, in Section 3.7 we also calculate a 3σ upper limit on the CO mass that could be in the outer belt and close in co-located with the hot dust.

3 DISC MODELLING

As the image reconstruction suffers from strong artefacts, we analyse the ALMA observations in the uv space and infer the millimetre-sized dust distribution by fitting the observed visibilities in the continuum with four different debris disc models: (1) an outer belt with a radial Gaussian surface density distribution to constrain the mean radius and width of the belt; (2) a self-stirred disc following the parametrization presented in Kennedy & Wyatt (2010) to study if the disc is consistent with such a scenario; (3) a LHB-like density distribution, which connects the outer belt with the inner regions with a surface density proportional to $r^{-1.5}$, that then we relax to a simple axisymmetric double power-law distribution; and (4) an eccentric outer belt to constrain the disc global eccentricity.

The models consist of a central star modelled using a Kurucz template spectrum³ (Kurucz 1979) with an effective temperature of 7000 K and a stellar radius of $1.75 R_\odot$ to fit the stellar flux (~ 250 μJy at 0.88 mm) as we impose the luminosity of the star to be $4\pi R_*^2 \sigma T_*^4$. The star is surrounded by a dusty disc with grains formed by astrosilicates (Draine 2003), amorphous carbon (Li & Greenberg 1997) and water ice (Li & Greenberg 1998), with mass fractions of 70, 15 and 15 per cent, respectively, with an internal density of 2.9 g cm^{-3} and mixed using the Bruggeman’s rule (Bohren & Huffman 1983) to match the composition used in Duchêne et al. (2014). We assume a Dohnanyi-like grain size distribution with a power-law index of -3.5 , with minimum and maximum grain size of 1.0 μm and 1.0 cm, respectively. This leads to a mass-weighted absorption opacity $\kappa_{\text{abs}} = 3.8$ $\text{cm}^2 \text{g}^{-1}$ at 0.88 mm, computed using the Mie theory code of Bohren & Huffman (1983). While (a_{min} , a_{max}), κ_{abs} and the derived total dust mass are highly dependent on our choice of the grain composition and size distribution, these assumptions have very little effect on the derived disc structure. Finally, we assume a Gaussian vertical mass distribution parametrized by a scaleheight H that scales linearly with radius as $H = hr$. As shown in Marino et al. (2016), this can be constrained by resolved ALMA observations of axisymmetric discs; therefore, we leave ‘h’ as a free parameter.

Using `radmc-3D`⁴ (Dullemond et al. 2015), we solve the thermal equilibrium of the mean dust species defined above, obtaining a temperature field that varies with radius as $42(r/150 \text{ au})^{-0.5}$ K,

³ <http://www.stsci.edu/hst/observatory/crds/k93models.html>

⁴ <http://www.ita.uni-heidelberg.de/~dullemond/software/radmc-3d/>

which is then used to produce synthetic images of the system at 0.88 mm. Finally, models are compared with the observations simulating model visibilities with the same uv -coverage and pointing offsets.

A Bayesian approach is used to constrain the different parameters of the disc models (details below), sampling the parameter space to recover the posterior distribution with the public PYTHON module `EMCEE` that implements the Goodman & Weare's Affine Invariant MCMC Ensemble sampler (Goodman & Weare 2010; Foreman-Mackey et al. 2013). Before running our MCMC routine, we reduced the original ALMA data averaging the visibilities with time and frequency bins of 3 min and 2 GHz, respectively. This considerably reduces the computational time of the MCMC routine without losing significant information (checked by comparing the S/N in the `CLEAN` images before and after averaging the data) and without producing a bandwidth or time smearing bigger than 0.15 arcsec along the ring. The posterior distribution is then defined as the product of the likelihood function and the prior probability distribution functions for each parameter, which we assume are uniform. The likelihood function is defined proportional to $\exp(-\chi^2/2)$, with χ^2 defined as

$$\chi^2 = \sum_i \frac{\|V_{\text{data},i} - V_{\text{model},i}\|^2}{\delta V_{\text{data},i}^2}, \quad (1)$$

where the sum goes over the 1.16×10^6 uv points of the observed visibilities, $v_{\text{data},i}$, previously averaged. The estimated error $\delta v_{\text{data},i}$ is calculated based on the intrinsic dispersion of the visibilities over one scan with the task `statwt` from `CASA` 4.4. In our priors, we impose a lower limit to the vertical aspect ratio, h , equivalent to 0.03. This is necessary as our model has a fixed grid with a vertical resolution of 2.3 au at 150 au ($h = 0.015$) around the mid-plane, chosen to reduce the computational time of our MCMC routine. We run `EMCEE` for 300–1000 steps using 50–180 *walkers*, depending on the model, obtaining auto-correlation lengths of $\lesssim 50$, small enough to have more than 300 independent sets of samples. The different models are detailed below and compared in Section 3.5 using the Bayesian information criterion (BIC; Schwarz 1978).

3.1 A radially symmetric belt

In order to estimate the mean radius and radial width of the outer belt, our first model consists of a belt with a surface density distribution that is parameterized with a Gaussian centred at r_0 and with a radial FWHM Δr as

$$\rho(r, z) = \rho_0 \exp \left[-\frac{4 \ln(2)(r - r_0)^2}{\Delta r^2} - \frac{z^2}{2H^2} \right], \quad (2)$$

where ρ_0 is defined to match the total dust mass, M_d , and $H = hr$ is the scaleheight. Then, the dust density distribution is defined by M_d , r_0 , Δr and h that we leave as free parameters. Two extra free parameters were defined to fit the disc inclination, i , and PA in sky. In Table 2, we summarize the best-fitting values and uncertainties. We find the disc mean radius is 152 ± 3 au and a radial FWHM of 46 ± 5 au, consistent with our previous estimate in Section 2.1.

We derive an inclination and PA of $35 \pm 2^\circ$ and $117 \pm 4^\circ$, respectively, which match the previous estimations by Lebreton et al. (2016) by fitting ellipses to *Herschel* observations ($i = 38.2 \pm 3.6$ and $\text{PA} = 116.2 \pm 1.1$), but our derived inclination is significantly smaller than $47 \pm 1^\circ$, the inclination derived by Duchêne et al. (2014) using the same *Herschel* data, but fitting a disc model to the observations and using a different data reduction. This difference could be due to the different methods used to derived the

Table 2. Belt model best-fitting values. Median \pm uncertainty based on the 16th and 84th percentile of the marginalized distributions. For parameters with distributions extending out to the minimum or maximum allowed values, a 1σ upper or lower limit is specified based on the 68th or 32nd percentile, respectively.

Parameter	Best-fitting value
M_d [M_\oplus]	0.014 ± 0.001
r_0 [au]	152 ± 3
Δr [au]	46 ± 5
h	< 0.13 (1σ)
PA [$^\circ$]	117 ± 4
i [$^\circ$]	35 ± 2

disc inclination, data reduction, or due to different PSFs as these can vary significantly between different *Herschel* observations (e.g. Kennedy et al. 2012), making their uncertainties larger than the ones quoted above. The inferred disc mean radius and radial width are overall consistent with their derived dust distribution, with differences due to the different models assumed. The total flux of the best-fitting model is 13.3 ± 1.0 mJy (excluding calibration uncertainties). This is higher than the measured flux from the `CLEAN` image (9.2 ± 0.5 mJy) and consistent with the total flux measured by SCUBA-2/JCMT. We also find that the posterior distribution of the aspect ratio h peaks at 0.10, $\sim 2\sigma$ above the lower limit in our prior distribution (0.03), but still consistent with 0.

A synthetic image, simulated ALMA image, and dirty map of the residuals of the best-fitting model are presented in Figs 6(a), (d) and (g), respectively. Despite the model being axisymmetric, the simulated ALMA image shows asymmetric structure along the belt, similar to the observed features in the ALMA image (see Fig. 1). The maxima along the minor axis and minima along the major axis are well reproduced; thus, the observed asymmetries are likely an artefact of the image reconstruction caused by a low S/N in the visibilities and the uv -sampling. After subtracting the model visibilities, the dirty map of the residuals shows no excess above 3σ that could be attributed to an overdensity in the belt or emission inside the cavity.

Similar to the analysis in Section 2.1, in Fig. 7 we compute the azimuthal profile of the residuals along the outer belt averaging between 130 and 175 au. The integrated flux of the residuals around the outer belt is 1.2 ± 0.3 mJy (correcting by the primary beam), an excess which is within the uncertainty of the flux in our model. At a PA of 290° , the residuals show an excess of $20 \mu\text{Jy beam}^{-1}$ (3σ). Moreover, the excess on the north-west half of the disc is 0.8 ± 0.2 mJy, while 0.4 ± 0.2 mJy on the opposite side of the disc. This is consistent with what we found in Section 2.1 and the $70 \mu\text{m}$ PACS image of the disc, and points to a slight excess of emission in the north-west side of the disc.

The best-fitting model has a reduced chi-squared $\chi_{\text{red}}^2 = 1.0037898$, with 6.54×10^6 different visibility measurements before averaging. This is used later to compare the goodness of fit of different models.

3.2 Self-stirred disc

The cavity and outer belt in η Corvi could be the result of a primordial depletion of solids from a few au up to 110 au, followed by an overdensity or belt of planetesimals with a peak at 150 au, like in a transitional protoplanetary disc (e.g. Espaillat et al. 2014). Alternatively, the current disc structure could just be the result of

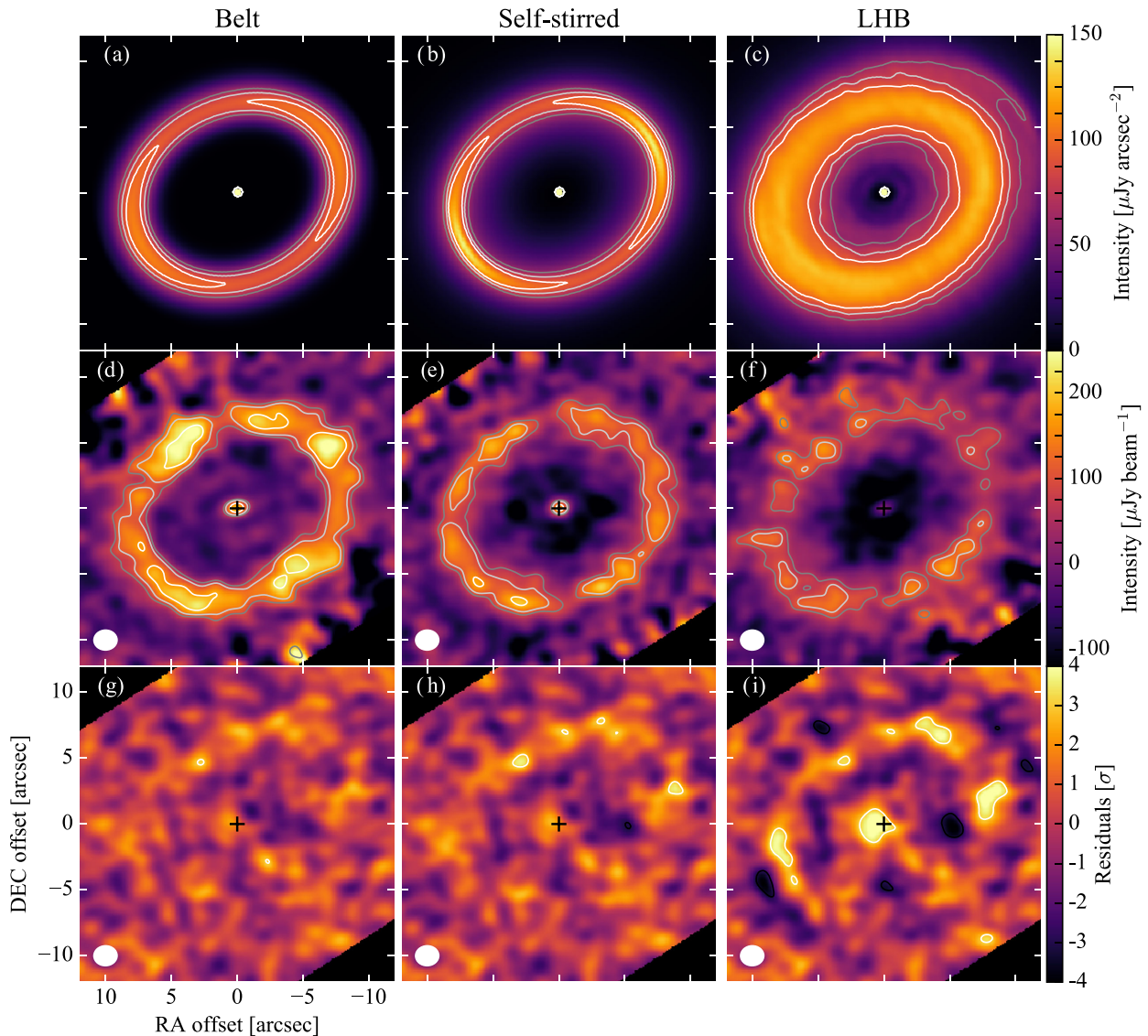


Figure 6. Simulated images at 0.88 mm. The first, second and third columns correspond to the best-fitting belt model (Section 3.1), best-fitting self-stirred disc model (Section 3.2) and LHB model (Section 3.3), respectively. First row: synthetic images of the disc. Contours represent 65, 80 and 95 $\mu\text{Jy arcsec}^{-2}$. Second row: primary beam corrected simulated CLEAN images using the same uv -sampling, adding Gaussian noise to the visibilities according to the variance of the observations, and uv -tapering the visibilities with a Gaussian of FWHM of 1.2 arcsec in sky. Contours represent two, three and five times the local noise level. Third row: dirty map of the residuals after subtracting the model visibilities from the ALMA observations. The noise level on the residuals is uniform and equal to 30 $\mu\text{Jy beam}^{-1}$ as they are not corrected by the primary beam. The black and white contours represent $\pm 3\sigma$. The beam size is represented by a white ellipse in the bottom left corner. The x - and y -axes indicate the offset from the stellar position in R.A. and Decl. in arcsec, i.e. north is up and east is left. The stellar position is marked with a black '+'. The noise level on the residuals is uniform and equal to 30 $\mu\text{Jy beam}^{-1}$ as they are not corrected by the primary beam.

the collisional evolution of a broad primordial disc of planetesimals being self-stirred as Pluto-sized objects are being formed at different epochs at different radii. In order to test the latter scenario and see if the disc morphology can be explained by self-stirring, we considered a second model that consists of a parametric self-stirred disc based on the work by Kennedy & Wyatt (2010). In this scenario, the surface density of solids evolves from a primordial disc of planetesimals to a stirred disc in collisional equilibrium as

$$\Sigma(r, t) = \begin{cases} \Sigma(r, 0) x_{\text{delay}} & t < t_{\text{stir}}(r) \\ \Sigma(r, 0) / \left[1 + \frac{t - t_{\text{stir}}(r)}{t_c(r)} \right] & t > t_{\text{stir}}(r), \end{cases} \quad (3)$$

where $\Sigma(r, 0)$ is the primordial surface density of solids assumed here to follow a power law, i.e. $\Sigma_0(r/r_0)^{-\gamma}$, and t is the age of the system (assumed to be 1.4 Gyr here). At each radius, the disc is stirred at epoch $t_{\text{stir}}(r)$ after which it is assumed to be in collisional equilibrium, with a collisional lifetime of the biggest planetesimals $t_c(r)$ at the initial epoch of the collisional cascade (i.e. after being stirred). Similar to Kennedy & Wyatt (2010), we also introduce a factor $x_{\text{delay}} \leq 1$ in equation (3) when $t < t_{\text{stir}}$ because the collisional cascade has not yet begun, thus the amount of mass in grains that contribute to the millimetre emission could be lower (different size distributions).

The time-scale at which Pluto-sized objects are formed depends on both the distance to the star and the surface density of solids at that

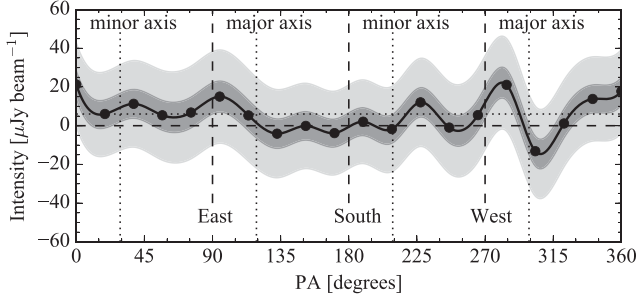


Figure 7. Intensity azimuthal profiles of the dirty map of the residuals of the best-fitting belt model, obtained averaging over elliptic annuli of semimajor axes between 6.8 and 9.8 arcsec (equivalent to 125 and 180 au) and over 18° wide wedges (centred at the black dots). The horizontal dotted line represents the mean intensity around the residuals in the outer belt. The light and dark grey areas represent the 68 and 99.7 per cent confidence region.

distance. Generally speaking, this time-scale will be proportional to the orbital period and inversely proportional to the primordial surface density of solids (e.g. Lissauer 1987), i.e. $t_{\text{stir}}(r) \propto r^{3/2}/\Sigma(r, 0)$. Because we aim to fit the observations, in our self-stirred model we use the following empirical relation

$$t_{\text{stir}}(r) = t_{\text{age}}(r/r_{\text{stir}})^{3/2+\gamma}, \quad (4)$$

where r_{stir} is defined as a reference radius where stirring is happening at the present epoch (t_{age}). With this parametrization the peak of the disc emission is at r_{stir} which is comparable to r_0 in the belt model. We can make an order of magnitude estimation of this time-scale extrapolating the time-scale at which Pluto formed (~ 40 Myr; see Brown 2002, and references therein) to 150 au using $\gamma = 1$. We find $t_{\text{stir}}(150 \text{ au}) = 1.5$ Gyr, consistent with simulations by Kenyon & Bromley (2008) (see their equation 41), and of the same order as the age of the system; therefore, we consider that the self-stirring scenario is plausible.

On the other hand, the collisional lifetime of the biggest planetesimals in the disc is (see Wyatt et al. 2007b)

$$t_c(r) \propto r^{7/3} D_c Q_D^{*5/6} \Sigma(r, 0)^{-1}, \quad (5)$$

where D_c is diameter of the biggest planetesimal, and Q_D^* is the disruption threshold of planetesimals, here assumed to be independent of size. The above expression can be rewritten as

$$t_c(r) = t_0(r/r_{\text{stir}})^{7/3+\gamma}, \quad (6)$$

where t_0 is defined as the collisional lifetime of the biggest objects at r_{stir} . The net result is that the surface density is proportional to $r^{7/3}$ when $r \ll r_{\text{stir}}$ and $r^{-\gamma}$ when $r > r_{\text{stir}}$, while its shape close to r_{stir} is determined by the ratio t_c/t_{stir} which is $\approx t_0/t_{\text{age}}$.

Then, the free parameters are the total mass of dust M_d , h , γ , x_{delay} , r_{stir} , t_0 , PA and i . The posterior distributions of the most relevant parameters are presented in Fig. 8 and in Table 3 we summarize the best-fitting parameter values and uncertainties. The total flux of the best-fitting model is 16.7 ± 2.3 mJy. From the best-fitting values of the self-stirred model, we find that $\gamma = 6.4 \pm 1.4$, $x_{\text{delay}} = 0.3 - 1.0$ (95.0 per cent confidence, with a marginalized posterior distribution that peaks at 1), and $t_0 < t_{\text{age}}$, i.e. $t_c < t_{\text{stir}}$ (99.7 per cent confidence). This means that the disc has sharp inner and outer edges [see fig. 2 in Kennedy & Wyatt (2010)]. The disc model image, simulated ALMA image and dirty map of the residuals are presented in Figs 6(b), (e) and (h), respectively. Negative and positive emission at 3σ levels appear close to the stellar position

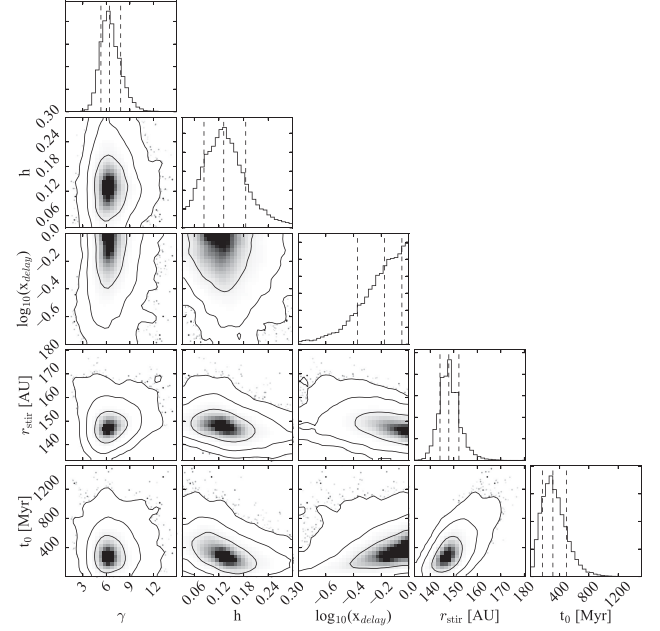


Figure 8. Posterior distribution of $h = H/r$, $\log_{10}(x_{\text{delay}})$, r_{stir} and t_0 from the self-stirred model. The vertical-dashed lines represent the 16th, 50th and 84th percentiles. Contours correspond to 68, 95 and 99.7 per cent confidence regions. This plot was generated using the PYTHON module *corner* (Foreman-Mackey et al. 2014).

Table 3. Self-stirred model best-fitting values. Median \pm uncertainty based on the 16th and 84th percentile of the marginalized distributions. For parameters with distributions extending out to the minimum or maximum allowed values, a 1σ upper or lower limit is specified based on the 68th or 32nd percentile, respectively.

M_d [M_\oplus]	0.019 ± 0.003
h	< 0.16 (1σ)
$\log_{10}(x_{\text{delay}})$	> -0.26 (1σ)
r_{stir} [au]	148 ± 4
t_0 [Myr]	300_{-140}^{+180}
γ	6.4 ± 1.4
PA [$^\circ$]	118 ± 4
i [$^\circ$]	34 ± 3

in the simulated ALMA image and dirty map of the residuals, respectively. However, these negatives are less significant in the belt model, which does not have any emission in the inner regions apart from the star (see Section 3.1). If the emission were really there, then it should appear brighter in the residuals of the belt model. We find the best-fitting model has a $\chi_{\text{red}}^2 = 1.0037958$, with 6.54×10^6 different visibility measurements.

Using equation (16) from Wyatt (2008) and the derived values of r_{stir} and t_0 , we can estimate the mean surface density ($\Sigma = M_{\text{tot}}/2\pi r dr$) or total mass in planetesimals (M_{tot}), assuming a maximum planetesimal size D_c of 1000 km and a power-law size distribution of solids with an exponent of -3.5 . We find

$$\Sigma_{r_{\text{stir}}, t=0} = 0.7 \left(\frac{r_{\text{stir}}}{150 \text{ au}} \right)^{7/3} \left(\frac{D_c}{1000 \text{ km}} \right) \left(\frac{Q_D^*}{200 \text{ JKg}^{-1}} \right)^{5/6} e^{-5/3} \times \left(\frac{M_\star}{1.4 M_\odot} \right)^{-4/3} \left(\frac{t_0}{300 \text{ Myr}} \right)^{-1}, \quad (7)$$

in $M_{\oplus} \text{ au}^{-2}$. This corresponds to a total mass of $3 \times 10^4 M_{\oplus}$ in the outer belt, which is too massive to be consistent with the self-stirred scenario. Considering only the mass on solids, this is equivalent to a Toomre Q parameter (Toomre 1964) of 1 assuming a vertical aspect ratio of 0.1; however, if we include the gas mass present during the protoplanetary disc phase ($\Sigma_{\text{gas}} \approx 100 \Sigma_{\text{solids}}$) we find that the disc would have been highly unstable under gravitational perturbations. The high value of M_{tot} is due to t_c at r_{stir} , i.e. t_0 , which is too short for 1000-km-sized bodies. This is because the model fits better the data if the outer belt is narrow, i.e. $t_0 \lesssim t_{\text{age}}$.

Combining the mass derived above as a function of the maximum planetesimal size, i.e. $M_{\text{solids}} = 3 \times 10^4 (D_c/1000 \text{ km}) M_{\oplus}$, with dust mass on grains smaller than 1 cm, i.e. $M_{\text{solids}} = 0.02 (D_c/1 \text{ cm}) M_{\oplus}$, we find a maximum planetesimal size of $D_c \sim 40 \text{ m}$, but this contradicts the hypothesis that the disc is stirred by the growth of planetesimals up to Pluto-sized bodies. The collisional time-scale could be longer (and so allow a larger maximum planetesimal size) if the age of the system is greater than 1.4 Gyr as it is the ratio between both that determines the shape of the surface density; however, to reconcile the maximum planetesimal size ($\sim 1000 \text{ km}$) and the disc mass, the age of the system should be ~ 100 times longer, which is impossible. Therefore, we conclude that self-stirring is unlikely to have produced the observed disc morphology in η Corvi. However, we cannot rule out that all the solids are smaller than 40 m (leading to a total mass of $\sim 1.3 M_{\oplus}$) if the disc is externally stirred, a possibility that is discussed in Section 4.1.1.

3.3 Late heavy bombardment

As the hot dust around η Corvi cannot be sustained by a collisional cascade *in situ*, Lisse et al. (2012) suggested that this system could be undergoing an instability similar to the LHB in the Solar system. The outward migration of Neptune after Jupiter and Saturn crossed the 1:2 resonance caused a massive delivery of planetesimals to the inner Solar system, high-frequency collisions with the Earth and Moon, and a population of eccentric and highly inclined objects in the Kuiper belt (Gomes et al. 2005). During such instability the disc could have specific observable features different from a scenario in which planets are in stable orbits for long time-scales. For example, Booth et al. (2009) showed that the Kuiper belt should be broad during the LHB (see fig. 1 therein) with a surface density profile approximated by a power law proportional to $r^{1.5}$ between 1 and 27 au and $r^{-4.8}$ between 38 and 106 au. Moreover, the disc could display asymmetries such as spiral arms or disc offsets with respect to the stellar position produced by a planet put on an eccentric orbit after the instability (see fig. 7 in Pearce & Wyatt 2014).

Fig. 9 shows the surface density of planetesimals during the LHB in the Solar system (at $t = 880 \text{ Myr}$ after the start of the simulation), obtained from N -body simulations from one of the Nice model runs (Gomes et al. 2005). As a first approximation we linearly scale the semimajor axis of the planetesimals orbits to match the location of the mean radius of η Corvi, which maintains unchanged the surface density proportional to $r^{1.5}$. This is not necessarily true given the large size ratio between the Kuiper belt and the η Corvi debris disc (40/150) and the different ways the time-scales involved depend on the semimajor axis of particles in the simulation. Therefore, N -body simulations tailored to η Corvi might be necessary; however, this first approximation can be used to compare the observations with an LHB-like event in which an outer belt is perturbed after a dynamical instability in the system, producing a shallow surface density distribution of $r^{1.5}$ extending from the outer belt down to the inner

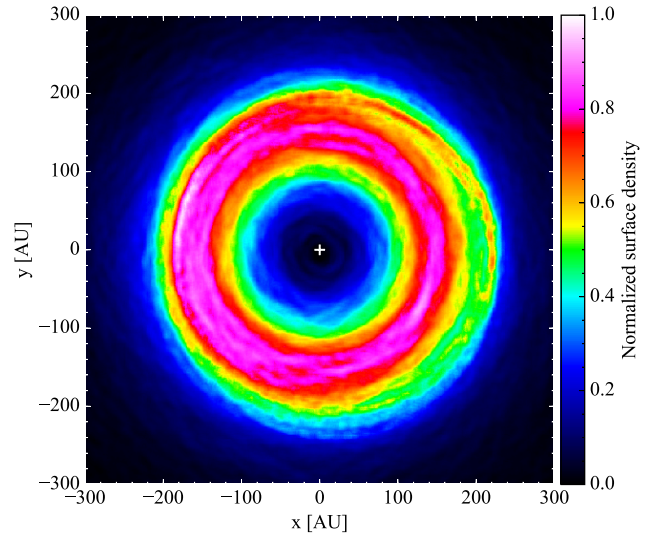


Figure 9. Normalized surface density of particles during the LHB computed from N -body simulations of one of the Nice models runs (Gomes et al. 2005). The particles from the simulation were duplicated assigning to each one a random anomaly in order to spread them around their orbits. Finally the particle's semimajor axes were scaled by 3.75 to match the size of the outer disc in η Corvi. The stellar position is marked with a white '+'.
Downloaded from https://academic.oup.com/mnras/article/465/3/2595/2420719 by guest on 28 January 2022

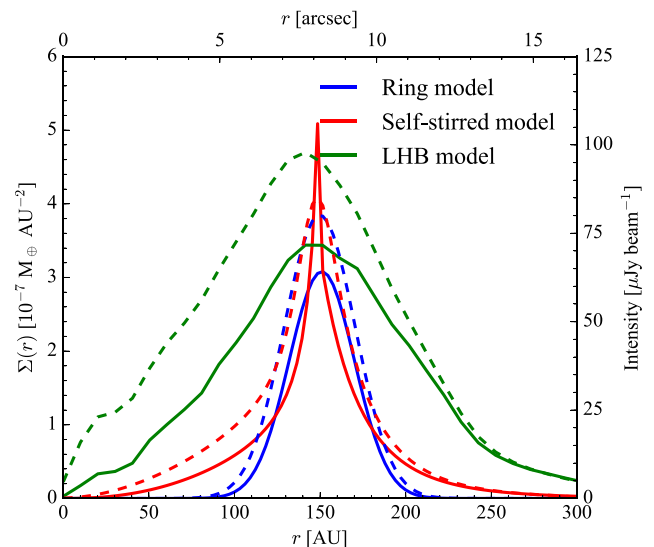


Figure 10. Dust surface density (continuous line) and surface brightness profiles convolved with a beam of 1 arcsec (dashed line) of the best-fitting belt, self-stirred and LHB models, represented in blue, red and green, respectively.

most regions (see Fig. 10). To smooth the derived surface density, we also randomly spread each particle around its orbit according to the velocity they have at each location. This is only valid if the collisional time-scales of the solids are longer than the orbital period, which is probably true for millimetre-sized grains given the low surface density of the disc. This technique also washes out any resonant structure that relies on the correlation between the mean longitude and the longitude of pericentre of a particle, although resonances may not be a strong feature at this stage of the evolution. Finally, we simulate images of the disc assuming that millimetre-sized grains, which dominate the continuum emission at millimetre

Table 4. Double power-law model best-fitting values. Median \pm uncertainty based on the 16th and 84th percentile of the marginalized distributions. For parameters with distributions extending out to the minimum or maximum allowed values, a 1σ upper or lower limit is specified based on the 68th or 32nd percentile, respectively.

M_d [M_\oplus]	0.016 ± 0.002
h	<0.15 (1σ)
r_c [au]	151 ± 4
α_{in}	$6.2^{+2.0}_{-1.3}$
α_{out}	$-7.5^{+1.3}_{-2.2}$
PA [$^\circ$]	119 ± 4
i [$^\circ$]	35 ± 2

wavelengths, have the same distribution as their parent bodies, as they are not affected by radiation pressure. We vary the disc flux to fit to the visibilities finding a best fit with a total disc flux of 39 ± 2 mJy ($0.048 \pm 0.002 M_\oplus$ of dust, assuming the same optical properties as the models described above). This is much higher and inconsistent with the total flux measured by SCUBA-2/JCMT and is required to fit the ALMA data because most of the emission is on large scales, and thus, resolved out. In Figs 6(c), (f) and (i), we present the synthetic continuum image at 0.88 mm, ALMA simulation and dirty map of the residuals after subtracting it to the observed visibilities. Despite the fact that the model surface density displays asymmetric features such as spiral arms, we find that the simulated observations are not sensitive enough to recover this structure, and thus, they are roughly consistent with an axisymmetric disc. However, the LHB best-fitting model fails to reproduce the observed surface brightness observed by ALMA as it is broader and fainter in the reconstructed image, despite requiring three times the flux measured by SCUBA-2/JCMT.

In order to place better constraints on the surface density exponent of a possible extended disc, we fit an axisymmetric model with a surface density defined as a double power law

$$\Sigma(r) = \begin{cases} \Sigma_0 (r/r_c)^{\alpha_{\text{in}}} & r < r_c \\ \Sigma_0 (r/r_c)^{\alpha_{\text{out}}} & r > r_c, \end{cases} \quad (8)$$

where r_c , α_{in} and α_{out} are free parameters, together with the total mass of dust in the disc, M_d , the vertical aspect ratio, h , and the PA and inclination of the disc in sky. In Table 4, we summarize the best-fitting values and uncertainties. We find $\alpha_{\text{in}} = 6.2^{+2.0}_{-1.3}$, with a 3σ lower limit of 3.3. Therefore, we conclude that the surface density of solids in the disc has to rise considerably steeply than that of $r^{-1.5}$ in the cavity towards the outer belt, discarding a LHB-like surface density and a highly scattered outer belt. The best-fitting model has a $\chi^2_{\text{red}} = 1.0037906$, with 6.54×10^6 different visibility measurements.

3.4 Eccentric belt

We also study the possibility of the belt being eccentric. This has two main effects: the centre of the belt is offset from the stellar position, and the azimuthal density profile changes as particles spend more time at the apocentre increasing its density relative to the pericentre. This is known as apocentre glow (Pan, Nesvold & Kuchner 2016). Therefore, we fit a modified belt model in which we replace ρ_0 and r_0 in equation (2) by

$$\rho_c = \rho_0 [1 - e \cos(f)], \quad (9)$$

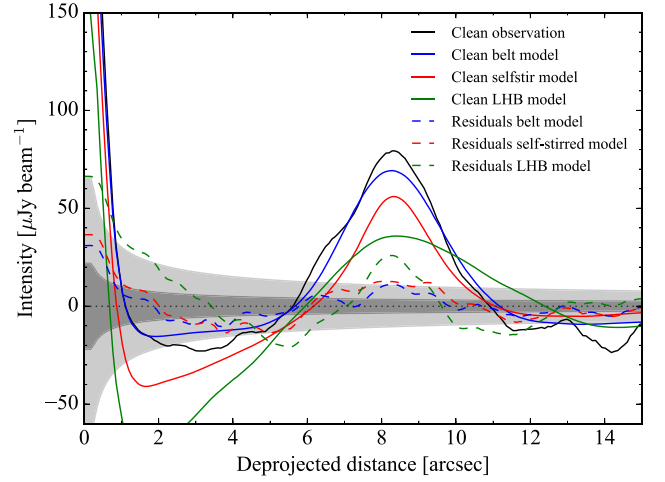


Figure 11. Azimuthally averaged intensity profiles obtained from CLEAN non-tapered images of simulated observations without noise using the best-fitting models (continuous lines) and from the non-tapered dirty map of the residuals after subtracting the best-fitting models (dashed). The blue, red and green lines represent the belt, self-stirred and LHB models, respectively. The η Corvi CLEAN azimuthally averaged profile is represented with a continuous black line. The light and dark grey areas represent the 68 and 99.7 per cent confidence region.

$$r_c = \frac{r_0(1 - e^2)}{1 + e \cos(f)}, \quad (10)$$

where e is the eccentricity of the belt and f is the true anomaly, i.e. the azimuthal angle in the plane of the disc measured from the direction of pericentre as seen from the stellar position. We maintain fixed the scaleheight to the best-fitting values presented above and we added as free parameters e and the PA of the pericentre, w , i.e. the angle in the plane of the sky between the north direction and that of the pericentre as seen from the stellar position, to have a total of seven free parameters. We initiated the MCMC using a uniform distribution of w from 0° to 360° and a normal distribution for e centred at 0 with a standard deviation of 0.03. We run 10 MCMC routines in parallel, each one with 18 walkers to ensure a good sampling of the parameter space. We find that the disc is consistent with being circular and from the posterior distribution of e ; we derive a 99.7 per cent upper limit of 0.05 (see Section 4.1.3 for implications of this upper limit). We find that the marginalized distribution of w is not uniform and constrained between -80° and 60° (99.7 per cent confidence), i.e. the pericentre if eccentric is more likely to be on the northern half of the disc. However, e still peaks at zero even for these values of w .

3.5 Model comparison

In Fig. 10, we compare the surface density and surface brightness profiles of the belt and self-stirred model using the best-fitting parameters defined above. They display strong differences in their surface density and brightness profiles, with the self-stirred and LHB models extending significantly inside 100 au and outside 200 au. Fig. 11 shows intensity radial profiles obtained by averaging azimuthally simulated CLEAN images of the best-fitting models without noise, and from the dirty maps of their respective residuals when comparing with the observations. The three models suffer from strong negative artefacts inside the cavity, with the LHB model

being the most extreme. Moreover, the self-stirred and LHB models appear dimmer on the simulated observation than it should based on the model (peak of 85 and 95 $\mu\text{Jy beam}^{-1}$ at 8 arcsec or 150 au, respectively). This is probably due to an insufficient number of short baselines to capture the broad emission. In the same figure, we notice that the negative artefacts on the CLEAN image are significantly reduced in the residuals below $\pm 3\sigma$ after subtracting the best belt model to the visibilities, as expected if they are artefacts created by the image reconstruction.

With the belt model we obtain the best χ^2 , followed by the double power-law model. In addition, to compare the goodness of fit of the three best-fitting models, it is useful to compute the BIC (Schwarz 1978) for each one, which penalizes for the number of free parameters. It is defined as $\chi^2 + k \log(N)$, where k is the number of free parameters (six for the belt model, eight for the self-stirred model and seven for the double power-law model) and N is the number of data points or visibilities. A model is more preferred when its BIC is lower, with a difference larger than 10 considered to be strong evidence (Kass & Raftery 1995). We find that the belt model's BIC is lower by ~ 40 compared to the self-stirred best model's BIC, and lower by 20 compared to the double power-law model. Thus, we conclude the simple Gaussian belt model gives a better fit to the observations, even with a lower number of free parameters.

3.6 Missed extended emission inside the belt

It is possible that there could be emission in the cavity missed by ALMA due to a low surface brightness or even due to an insufficient number of short baselines to recover more extended emission. Assuming a constant dust opacity with radius, we can estimate how much dust mass could be hidden at an undetectable level between the star and the belt at 150 au. The maximum surface density (3σ upper limit) can be defined as

$$\Sigma(r) = \frac{\delta I(r)}{\kappa_{\text{abs}} B_{\nu}(T(r))}, \quad (11)$$

where $\kappa_{\text{abs}} = 3.8 \text{ cm}^2 \text{ g}^{-1}$ is the absorption opacity of grains in our models and $\delta I(r)$ is the 3σ uncertainty of the azimuthally averaged intensity profile, computed considering the noise in the image space, as well as the apodization by the primary beam. We also assumed $T(r) = 42(r/150 \text{ au})^{-0.5} \text{ K}$, derived from the dust temperature in our models described above (assuming a uniform grain size distribution and composition in the disc). Integrating $\delta I(r)$ or $\Sigma(r)$, we find a total missing flux $\lesssim 3.4 \text{ mJy}$ or a possible hidden dust mass $\lesssim 2.4 \times 10^{-3} M_{\oplus}$ in the cavity (3σ limits).

However, this approach does not take into account the uv -filtering that could be present due to missing short baselines, as the maximum recoverable scale is ~ 7 arcsec. Our observations are blind to structure of that size or bigger. To study this effect and get a more accurate constraint on the possible hidden emission inside the cavity, we added a second component to the simple belt model described in Section 3.1 and fit this to the observed visibilities. The second component is defined with a surface density proportional to r^{α} between 1 and 150 au (inside the belt mean radius), where we leave α as a free parameter that can vary between -5 and 5 , together with the total dust mass of the second component, M_{d2} . In Fig. 12, we present the distribution of α , the total dust mass M_{d2} and flux of the second component. We find a 3σ upper limit of $2.7 \times 10^{-3} M_{\oplus}$ for M_{d2} and 3.2 mJy for the flux of the second component. This is similar to our previous analytic estimate, which rejects the hypothesis of extended disc emission in the cavity at detectable levels, but

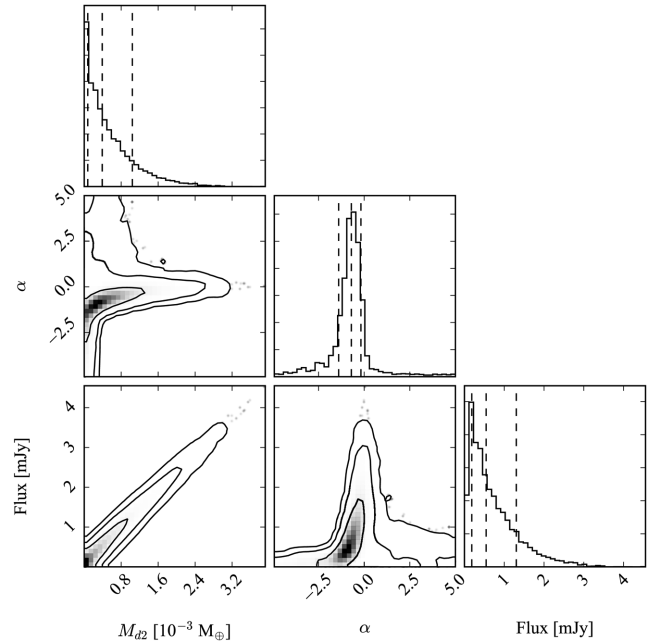


Figure 12. Posterior distribution of α , M_{d2} and the total disc flux of the second inner component. The vertical-dashed lines represent the 16th, 50th and 84th percentiles. Contours correspond to 68, 95 and 99.7 per cent confidence regions. This plot was generated using the PYTHON module *corner* (Foreman-Mackey et al. 2014).

filtered out by missing short baselines. It is worth noting that this parametric method to constrain the flux from the cavity assumes a power-law surface density distribution.

3.7 CO mass constraints

As shown by Matrà et al. (2015) local thermodynamic equilibrium (LTE) does not necessarily apply to the low-density environments of debris discs. Thus, when deriving gas masses from observed CO emission or even upper limits from non-detections, it is necessary to consider non-LTE effects when the densities of the main collisional partners, which we assume to be electrons, are not high enough. This choice is justified because if CO gas of secondary origin is present, electrons should be released from carbon ionization after the photodissociation of CO, dominating the collisional excitations and de-excitations of the CO rotational levels. However, we stress that the mass limits derived in the radiation-dominated regime (low electron densities) and in LTE (high electron densities) are independent of the specific collisional partner. Similar to Fomalhaut (Matrà et al. 2015), the radiation at 345 GHz in the disc is dominated by the CMB photons ($J_{\nu} = 1.4 \times 10^8 \text{ Jy sr}^{-1}$) as the mean dust intensity inside the belt is $\lesssim 8 \times 10^7 \text{ Jy sr}^{-1}$ (calculated from our best-fitting model in Section 3.1) and the stellar flux is $\sim 10^8 \text{ Jy sr}^{-1}$ at 5 au, which decreases steeply as r^{-2} and becomes negligible at 20 au. We also neglect the flux from the hot dust, as it is highly unconstrained at this wavelength. We use the code developed by Matrà et al. (2015) that computes the population of the rotational levels in the non-LTE regime to derive CO total fluxes and gas masses for different electron densities (n_{e^-}) and gas kinetic temperatures (T_k), assuming the emission is optically thin.

From the total flux of $38 \pm 9 \text{ mJy km s}^{-1}$ measured between 15 and 37 au (see Section 2.2), we can estimate the CO gas mass located around 20 au considering different n_{e^-} and T_k (20–300 K).

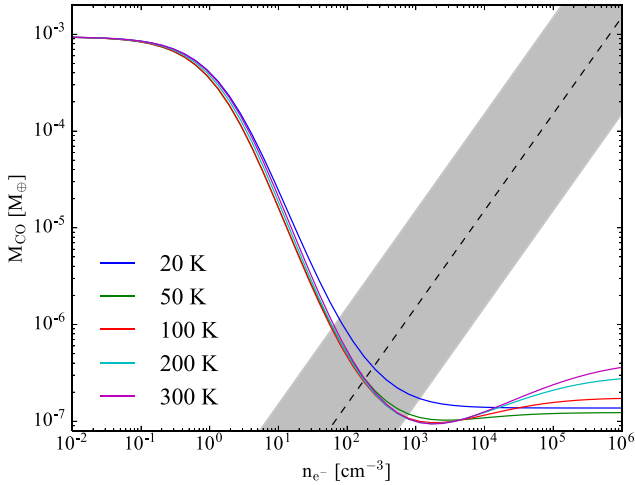


Figure 13. CO gas mass estimate of the detection at ~ 20 au for different gas kinetic temperatures and electron densities (n_{e^-} , main collisional partner). The dashed line corresponds to the CO gas mass assuming an abundance ratio of neutral carbon and CO of 100 and a carbon ionization fraction of 0.5. The grey-shaded region represents a factor of 10 of uncertainty on the CO and electron abundance ratio.

This is shown in Fig. 13. As expected from the work by Matrà et al. (2015), the mass of CO is highly unconstrained without any knowledge of n_{e^-} . M_{CO} could easily be between $\sim 10^{-3} M_{\oplus}$, in the radiation-dominated regime (low n_{e^-}), and $10^{-7} M_{\oplus}$, in LTE (high n_{e^-}). On the other hand, different gas kinetic temperatures can change M_{CO} by a factor of a few when close to LTE.

However, in the secondary origin scenario electrons are a byproduct of CO photodissociation and carbon ionization; therefore, n_{e^-} can be linked to M_{CO} . In fact, equation (14) in Matrà et al. (2015) shows that

$$M_{\text{CO}} = \frac{n_{\text{C}}}{n_{\text{C}^+}} \frac{n_{\text{CO}}}{n_{\text{C}}} m_{\text{CO}} V_{\text{disc}} n_{e^-} \approx 0.01 m_{\text{CO}} V_{\text{disc}} n_{e^-}, \quad (12)$$

where m_{CO} is the mass of the CO molecule and v_{disc} is the volume of the disc from 15 to 37 au assuming a vertical aspect ratio of 0.1. Based on previous studies of the β Pictoris disc, we assume $n_{\text{C}}/n_{\text{C}^+} = 1$ (Cataldi et al. 2014) and $n_{\text{CO}}/n_{\text{C}} = 1/100$ (Roberge et al. 2000) as first approximation. Therefore, if the CO gas is of secondary origin, its mass is defined roughly by the intersection of the dashed and continuous lines in Fig. 13, i.e. $M_{\text{CO}} \sim 3 \times 10^{-7} M_{\oplus}$. This could vary by a factor of a few given the flux uncertainty and the assumptions on v_{disc} , the carbon ionization and CO/C abundance ratio. These uncertainties are represented by the grey-shaded region defined between 0.1 and $10 M_{\text{CO}}$. We also find a CO mass-loss rate of $\sim 3 \times 10^{-9} M_{\oplus} \text{ yr}^{-1}$, as CO photodissociates in a time-scale of 120 yr due to the interstellar UV radiation field (Visser, van Dishoeck & Black 2009), which is of the same order as the hot dust mass-loss rate ($\sim 3 \times 10^{-9} M_{\oplus} \text{ yr}^{-1}$; Wyatt et al. 2010). Possible origins of the CO gas are discussed in Section 4.2.

Based on the flux upper limits derived in Section 2.2, we can also estimate a mass upper limit on the CO gas mass that could be in the outer belt or co-located with the hot dust. In Fig. 14, we present the 3σ mass upper limits for the CO in the outer belt, considering different T_{k} (10–150 K, a more appropriate range for T_{k} at 150 au) and electron densities. Similar to the derived mass above, the CO gas mass upper limit is not well constrained and strongly depends on the density of electrons in the disc varying by 4 orders of magnitude from 10^{-7} to $10^{-3} M_{\oplus}$. Using equation (12)

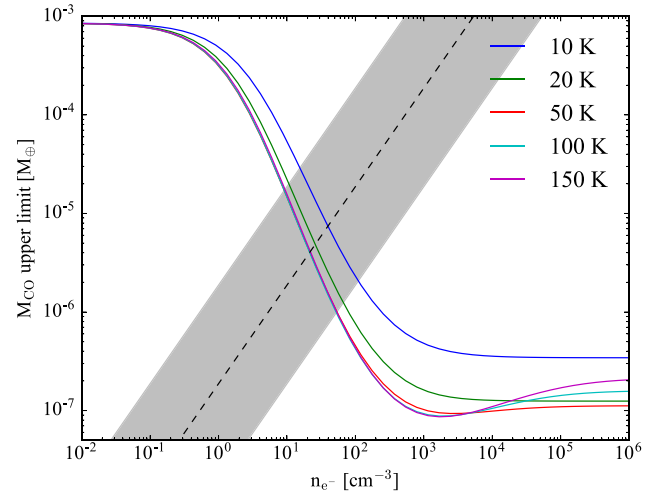


Figure 14. CO gas mass upper limits in the outer belt for different gas kinetic temperatures and electron densities (n_{e^-} , main collisional partner). The dashed line corresponds to the mass upper limit of CO gas assuming an abundance ratio of neutral carbon and CO of 100 and a carbon ionization fraction of 0.5. The grey-shaded region represents a factor of 10 of uncertainty on the CO and electron abundance ratio.

and the volume of our best-fitting belt model, we can estimate the expected density of electrons for a given CO gas mass assuming the same carbon ionization and C/CO abundance ratio observed in β Pic. This is represented with a dashed line. As the C/CO abundance and carbon ionization ratio could be different than in β Pic, we represent these uncertainties with the grey-shaded region defined between 0.1 and $10 M_{\text{CO}}$. The intersection between the dashed line and the continuous lines in Fig. 14 gives the best mass upper limit in the secondary origin scenario, which is $4 \times 10^{-6} M_{\oplus}$ for $T_{\text{k}} = 50$ K. The CO mass could be higher than this limit, but this requires a low abundance of e^- , which would be unlikely given the derived mass of CO, which would photodissociate producing carbon that would get ionized releasing further e^- (Kral et al. 2016).

Similarly, we calculate mass upper limits for the CO co-located with the hot dust using the 3σ flux upper limit ($3 \times 11 \text{ mJy km s}^{-1}$), considering different T_{k} (100–2000 K, a more appropriate range for T_{k} at a few au) and including the stellar flux at 345 GHz and at a radius of 1 au (important for the radiation-dominated regime). This is shown in Fig. 15. We also overlay in dashed and dotted black lines the mass of CO gas as a function of the electron density assuming the same carbon ionization fraction and C/CO abundance ratio as in β Pic. The dashed line corresponds to a disc with uniform surface density that extends from 1 to 10 au in radius, while the dotted line represents a scenario in which most of the emission comes from a narrow ring between 0.9 and 1.1 au. Moreover, as the C/CO abundance and carbon ionization ratio could be different than in β Pic, we represent these uncertainties with a grey-shaded region defined between $0.1 M_{\text{CO}}^{\text{narrow}}$ and $10 M_{\text{CO}}^{\text{broad}}$. The intersections between the dashed and dotted lines with the continuous line give the best estimate of the CO mass upper limit assuming a secondary origin as in β Pic. These two cases can be thought as extreme cases, with the narrow ring scenario having the most conservative upper limit of $\sim 5 \times 10^{-7} M_{\oplus}$ for $T_{\text{k}} = 500$ K, roughly the equilibrium temperature at 1 au. This limit is of the order of the CO gas mass derived before located at ~ 20 au. However, more CO gas could be hidden if it were distributed in an optically thick narrow ring. In the same figure, we added the mass of CO at which the CO line

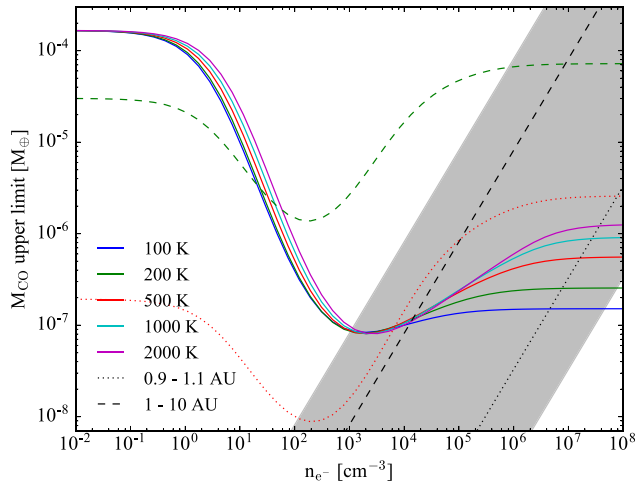


Figure 15. Mass upper limits of CO gas co-located with the hot dust for different gas kinetic temperatures and electron densities (n_{e^-} , main collisional partner). The dashed and dotted black lines correspond to the mass upper limit of CO gas assuming a narrow ring and a broad inner disc, respectively, and an abundance ratio of neutral carbon and CO of 100 and a carbon ionization fraction of 0.5. The dashed and dotted curves represent the mass of CO gas at which the line (3–2) becomes optically thick ($\tau = 1$) for a thin ring with $T_K = 500$ K (red) and a broad inner disc with $T_K = 200$ K (green). The grey-shaded region represents a factor of 10 of uncertainty on the CO and electron abundance ratio, considering a range of volumes from a narrow to a broad inner disc.

becomes optically thick (mean $\tau_\nu = 1$ across the line width), which is represented in red dotted and green-dashed lines for the two scenarios detailed above. We find that the upper limits are optically thin in the regime we are interested (secondary origin), unless the CO gas electron density is very low and the CO in the disc is far from LTE.

If CO is released in collisions of icy planetesimals, e.g. releasing CO gas trapped inside them or by exposing icy surfaces that can sublimate via thermal or photodesorption, then the rate at which CO gas is produced in the disc is given by

$$\dot{M}_{\text{CO}}^+ = f_{\text{CO}} \dot{M}, \quad (13)$$

where f_{CO} is the mass ratio of CO in planetesimals and \dot{M} is the mass-loss rate of planetesimals. In steady state, \dot{M}_{CO}^+ is equal to the rate at which CO is lost in the disc, i.e. $M_{\text{CO}}/\tau_{\text{CO}}$, where τ_{CO} is the photodissociation time-scale given by the interstellar UV radiation field (~ 120 yr; Visser et al. 2009). Using equations (15) and (16) from Wyatt (2008), the fractional luminosity of the outer disc ($\sim 2 \times 10^{-5}$; Duchêne et al. 2014), its mean radius and width derived in Section 3.1, and assuming mean planetesimal eccentricities of 0.05 and a uniform planetesimal disruption threshold (Q_{D}^*) of 200 J kg^{-1} , we can estimate the outer disc mass-loss rate and what would be the CO gas mass in the outer belt for CO mass fractions of planetesimal of 16 per cent (maximum fraction derived in Solar system comets; Mumma & Charnley 2011). We find that for these parameters, $\dot{M} \sim 10^{-3} M_{\oplus} \text{ Myr}^{-1}$ (or $\sim 4 \times 10^{-5} M_{\oplus} \text{ Myr}^{-1}$ for $Q_{\text{D}}^* \sim 10^4 \text{ J kg}^{-1}$) and $M_{\text{CO}} \sim 3 \times 10^{-8} M_{\oplus}$ or much lower if we consider higher disruption thresholds or lower abundances of CO in planetesimals. This mass of CO gas is much lower than our upper limit of $5 \times 10^{-6} M_{\oplus}$ derived above. The non-detection in the outer belt is therefore consistent with Solar system comet compositions.

On the other hand, the inner disc possesses a fractional luminosity of $\sim 3 \times 10^{-4}$ (Duchêne et al. 2014). Under the same assump-

tions detailed above and including the stellar radiation, we find that for a narrow ring $\dot{M} \sim 2 M_{\oplus} \text{ Myr}^{-1}$ and there should be $2 \times 10^{-5} M_{\oplus}$ of CO gas, far above the upper limit derived above for the inner disc. In fact, such a massive CO ring would be optically thick ($\tau_\nu \sim 7$). If we consider a broad inner disc spanning from 1 to 10 au, this limit decreases to $2 \times 10^{-6} M_{\oplus}$ ($\dot{M} \sim 0.1 M_{\oplus} \text{ Myr}^{-1}$), but still above the upper limit on the broad inner disc scenario. However, this prediction can be pushed down by increasing the disruption threshold or decreasing the abundance of CO trapped in planetesimals below 4 per cent (still consistent with Solar system comets, $f_{\text{CO}} = 0.3$ –16 per cent; Mumma & Charnley 2011). In fact, a low fraction of CO gas trapped in planetesimals is expected if volatiles have been lost at ~ 20 au on their way in from the outer belt (see Section 4.2).

4 DISCUSSION

4.1 Hidden planet(s)

4.1.1 Belt or self-stirred disc

In Section 3, we found that the disc continuum emission is consistent with a belt at 150 au and given the visibility uncertainties and insufficient short baselines in our ALMA data, the Gaussian belt model with three free parameters to describe the surface density, gives the best fit and it is not necessary to invoke a more complex model such as the self-stirred disc with two more free parameters. Moreover, we found that the derived collisional time-scale of the biggest bodies in the self-stirred scenario, which controls the width of the observed disc, is too short for a Pluto-sized body. However, it could be that the primordial disc of planetesimals was narrow. Then, it is no longer necessary that the stirring time-scale at 150 au (i.e. the age of the system) is longer than the collisional lifetime of the largest planetesimal, i.e. $t_0 \gtrsim t_{\text{age}}$, to produce a narrow debris belt as the primordial disc was already narrow; therefore, the outer belt could still be self-stirred. A narrow distribution of planetesimals in the outer belt, however it is stirred, could be due to a local enhancement of solids at ~ 150 au caused by the presence of a snow line of a specific volatile species that enhanced dust growth, or due to the presence of a nearby planet truncating the inner edge of the outer disc. In the latter scenario the planet could have stirred the disc before self-stirring takes place (Mustill & Wyatt 2012). It could also be the case that the outer belt formed narrow without being truncated by a nearby planet, but that a massive planet closer in stirred the outer belt before self-stirring could take place.

Alternatively, the morphology could be due to radial dust trapping of solids in pressure maxima at the edge of a gap or cavity during the protoplanetary disc phase (i.e. when this would have been classified as a transitional disc), where planetesimals could have grown. This can be produced by the presence of a massive planet that opens a gap in the disc (e.g. Pinilla, Benisty & Birnstiel 2012), located around 100 au in the case of η Corvi. For example HD 142527 has both an inner and an outer disc, with a cavity in both dust and gas extending from 10 au out to ~ 140 au (Fukagawa et al. 2006; Casassus et al. 2012). Although that system has a low-mass companion close in, it cannot have truncated the inner edge of the outer disc (Lacour et al. 2016). Thus, single or multiple planets have been proposed to explain both the large cavity and the transport of gas from the outer to the inner disc (as suggested by ALMA observations; Casassus et al. 2013; Casassus et al., 2015), necessary to maintain the accretion rate that otherwise would deplete the inner disc in less than a year (Verhoeff et al. 2011). Similarly, to explain the hot dust

in η Corvi a planetary system is required passing in material from its outer belt. Such a planetary system would probably stir the disc before self-stirring or the formation of a Pluto-sized object takes place (see Section 4.1.4).

4.1.2 From the outer to the inner disc

The two-component debris disc around η Corvi presents a challenge to any theoretical predictions of debris discs as its hot dust cannot be explained by a collisional cascade *in situ* as the system is too old ($\gtrsim 1$ Gyr). Moreover, spectroscopic features of the hot dust suggest that it was formed farther out, probably in the outer belt. P-R drag alone is incapable of transporting enough dust from the outer belt to the inner regions; therefore, a planetary system scattering material from the outer belt is required. In Section 1, we identified three possible scenarios to explain the hot dust in this system: (1) LHB-like instability, (2) a stable planetary system scattering material and feeding a collisional cascade closer in, and (3) a stable planetary system scattering planetesimals that collide with a planet within a few au. These new ALMA observations have shown that it is unlikely that the system is going through an instability such as the LHB (scenario 1). Such a scenario should leave asymmetric signatures, such as spiral arms or stellar-disc offsets (similar to the secular effect of an eccentric planet; Pearce & Wyatt 2014), and a broad outer belt (see Fig. 9 from this work and fig. 1 in Booth et al. 2009) during the evolution of the system. Given the rms achieved per beam in these ALMA observations, we cannot discard asymmetric features of the size of a few beams as they would not appear at a significant level (compare Figs 6c and 6f). However, we found that the outer belt is narrower compared with the LHB scenario (See Section 3.3) or it has a much steeper surface density slope within 150 au, and that it has a small global eccentricity, below 0.05. Thus, it seems unlikely that a dynamical instability in the system similar to the LHB is responsible for the hot dust excess. The outer belt has more likely retained a stable configuration over Gyr time-scales where icy material from the outer belt is being passed in to the inner regions (scenarios 2 and 3).

Bonsor & Wyatt (2012) and Bonsor et al. (2012) explored the limits at which multiple planets on circular orbits within 150 au can scatter particles inwards from the outer belt. The second study showed that it is difficult for planets more massive than Neptune to transport high levels of material to the inner planetary system, particularly after Gyr. This is based on the clearing of the planet's chaotic zone of material. However, if this material is replenished, planet scattering can sustain the hot dust. This can be done if the putative planet is migrating outwards into the outer belt (e.g. by planetesimal scattering; Bonsor et al. 2014).

Alternatively, solids could migrate inwards from the outer belt, e.g. via scattering with a low-mass planet located in the middle of the outer belt, through secular interactions with planets in the system, or by P-R drag transporting small dust from the outer belt, that then could fall into the chaotic zone of another planet located in the cavity and possibly continue migrating inwards. The planet in the middle of the belt should have a mass small enough such that the clearing time-scale of its chaotic zone is significantly longer than the age of the system, i.e. $\lesssim 7M_{\oplus}$ (see equation 3 in Shannon et al. 2016), as the observed outer belt shows no evidence of a gap or being cleared. Then, the icy material scattered from the outer belt to the inner regions could feed the hot dust via mutual destructive collisions of dust and planetesimals (scenario 2), or as a product of giant impacts on a planet close which would release large amounts

of dusty debris (scenario 3). Although the exact rate at which this material is transported and, thus, its radial distribution are unknown, in Section 3.6 we studied the possibility of a shallow component in the disc with different surface density distributions, connecting the outer belt with the hot dust region. We constrained the surface density distribution as a function of its slope and total dust mass. These limits can be used in the future to test hypotheses of planet configurations that can deliver material inward from the outer belt to the inner regions. For example, for a surface density increasing with radius as r^2 in the cavity, it cannot contain more dust mass than $8 \times 10^{-4} M_{\oplus}$ (assuming $\kappa_{\text{abs}} = 3.8 \text{ cm}^2 \text{ g}^{-1}$) or a total flux of 1 mJy.

Moreover, if the transport of material is in steady state, we can place a lower limit on the rate at which solids are migrating inwards by equating the hot dust mass-loss rate with the inward flux of solids. The first was estimated to be $\sim 3 \times 10^{-9} M_{\oplus} \text{ yr}^{-1}$ (Wyatt et al. 2010). This implies that if fed from the outer belt, this has lost at least $\sim 4 M_{\oplus}$ in the last 1.4 Gyr. On the other hand, the inward flux of solids can be expressed as

$$\dot{M}_{\text{hot}}^+ = 2 \pi r \Sigma(r) v_r(r), \quad (14)$$

where $\Sigma(r)$ is the surface density of dust in the cavity and v_r is the migration rate from the outer belt to the hot dust location. Here we assume $\Sigma(r) \propto r^{-1}$ and equal to $10^{-8}(r/100 \text{ au})^{-1} M_{\oplus} \text{ au}^{-2}$, equivalent to our upper limit of the total dust mass in the cavity ($10^{-3} M_{\oplus}$; see Section 3.6). Using the lower limit on \dot{M}_{hot} and upper limit on $\Sigma(r)$, we find that $v_r \gtrsim 5 \times 10^{-4} \text{ au yr}^{-1}$, i.e. a total migration time of 0.25 Myr from 100 to 1 au, assuming a surface density distribution proportional to r^{-1} . This lower limit [and others for different $\Sigma(r)$] can be tested by N -body simulations to assess scenarios 2 and 3 that could transport material from the outer belt to the inner regions producing the hot dust.

4.1.3 Constraints on a hidden planet at the disc inner edge

Although the depletion of dust interior to the outer belt and the high hot dust excess in η Corvi hint at the presence of stellar companions or planets, searches for them have not been successful. RV studies have discarded close in companions down to the mass of 6 Jupiter masses with a period shorter than 2000 d or with a semimajor axis less than 3 au (Lagrange et al. 2009; Borgniet et al. 2016). *Chandra* and *Spitzer* IRAC observations have also discarded the presence of a sub-stellar companion that could explain the unusually high X-ray luminosity of this old system (Marengo et al., in preparation). However, given the new constraints on the disc eccentricity, mean radius and width, we can put new constraints on a hidden planet. Assuming there is a single planet inside the η Corvi cavity, it cannot have a large eccentricity, e_{plt} , as an eccentric planet would impose a forced eccentricity, e_f , on the disc through secular interactions. This forced eccentricity must be lower than 0.05, the upper limit derived in Section 3.1 for the disc eccentricity. The relation between both eccentricities can be obtained from the disturbing function. Here we adopt the expression with no restriction in e_{plt} , based on equation (8) in Mustill & Wyatt (2009)

$$e_{\text{plt}} = -\frac{5\alpha}{8e_f} + \sqrt{\left(\frac{5\alpha}{8e_f}\right)^2 + 1}, \quad (15)$$

where α is equal to the ratio of the semimajor axis of the planet, a_{plt} , and the disc, $a_{\text{disc}} = 152 \text{ au}$.

We further assume that this planet is also responsible for truncating the outer disc and defining its inner edge, a_{in} , e.g. through direct

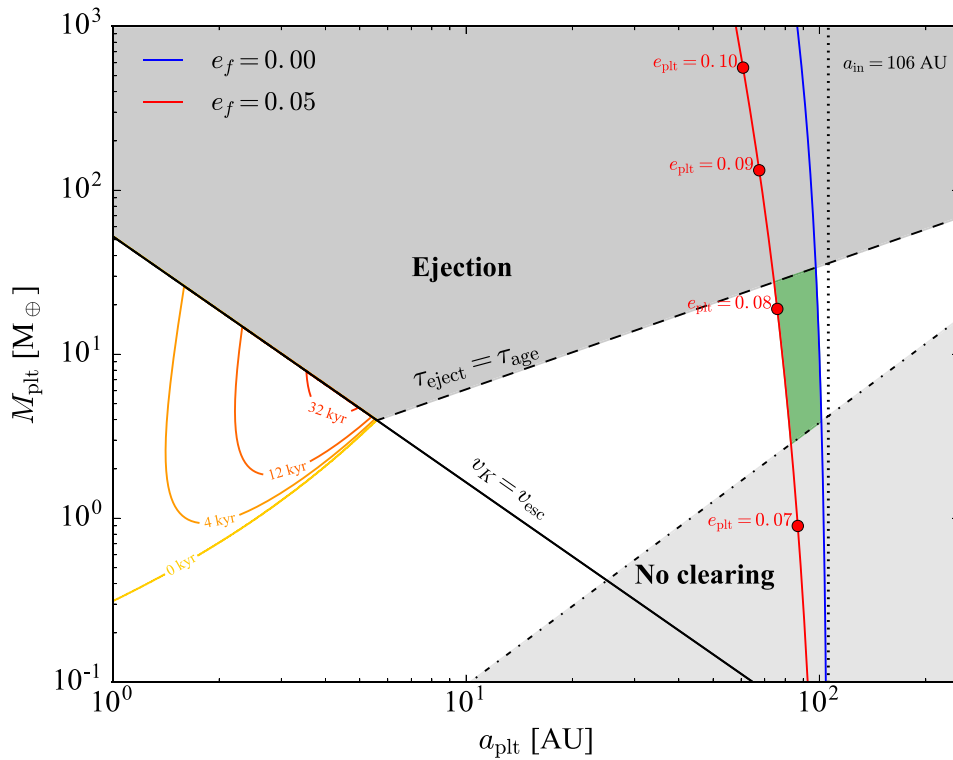


Figure 16. Constraints of the mass and semimajor axis of a perturbing planet in η Corvi. The blue and red lines are defined by equation (16) using a forced eccentricity of 0 and 0.05, respectively. Equation (18) is represented by a continuous black line, while equation (19) is represented by a black-dashed line. The mass of the planet to clear its chaotic zone on a time-scale equal to the age of the system (~ 1.4 Gyr) is represented by a dash-dotted line. The red dots display the eccentricity of the planet that varies along the red curve, increasing with M_{plt} . The inner edge of the disc is also shown with a dotted vertical line at 106 au. The grey regions show excluded regions where the planet would be too massive ejecting most of the material it encounters or not massive enough to stir the disc. In green we highlight the region where M_{plt} and a_{plt} meet all the conditions above. The yellow, orange and red contours represent different combinations of M_{plt} and a_{plt} in which a giant impact would produce debris that can remain above a fractional excess of 0.5 at $20 \mu\text{m}$ for a certain time-scale.

scattering and overlap of mean motion resonance in the so-called chaotic zone. The width of this zone has been estimated analytically for both small (equation 56 in Wisdom 1980) and high eccentricities (equation 10 in Mustill & Wyatt 2012), which we can use to relate the mass of the planet (M_{plt}) and its semimajor axis

$$M_{\text{plt}}(a_{\text{plt}}, e_f) = \begin{cases} \left(\frac{a_{\text{in}} - 1}{1.3} \right)^{7/2} M_{\star} & e_{\text{plt}} < e_{\text{crit}} \\ \left(\frac{a_{\text{in}} - 1}{1.8} \right)^5 e_{\text{plt}} M_{\star} & e_{\text{plt}} > e_{\text{crit}}, \end{cases} \quad (16)$$

where $a_{\text{in}} = r_0 - \Delta r = 106$ au, $M_{\star} \sim 1.4 M_{\odot}$ and e_{crit} is the critical eccentricity at which e_{plt} needs to be considered for the size of the chaotic zone (equation 11 in Mustill & Wyatt 2012), which for a Neptune mass planet is ~ 0.002 . Equations (15) and (16) define a surface in e_f versus a_{plt} versus M_{plt} space where this planet could reside. In Fig. 16, we present M_{plt} as a function of a_{plt} for $e_f = 0$ and 0.05 in continuous blue and red lines, respectively. With red dots we indicate the eccentricity of the putative planet along the $M_{\text{plt}}(a_{\text{plt}})$ curve. Both lines are nearly vertical and the region between them defines where a planet defining the outer belt's inner edge could lie.

However, a low-mass planet would clear its chaotic zone on time-scales of the order or even longer than the age of the system. We can use equation (3) in Shannon et al. (2016) which defines the clearing time-scale of the chaotic zone as a function of the planet mass and semimajor axis, to estimate the minimum mass of the

planet sculpting the inner edge

$$M_{\text{plt}}(a_{\text{plt}}) = 4 \left(\frac{t_{\star}}{1.4 \text{ Gyr}} \right)^{-1} \left(\frac{a_{\text{plt}}}{100 \text{ au}} \right)^{1.6} \left(\frac{M_{\star}}{1.4 M_{\odot}} \right)^{-1/2} [M_{\oplus}]. \quad (17)$$

A planet below this mass limit will not clear its chaotic zone fast enough to truncate the inner edge of the outer belt. Therefore, the planet sculpting the outer belt should lie between 60 and 110 au and have a mass higher than $3 M_{\oplus}$.

4.1.4 Maximizing the inward flow

As commented before, if material from the outer belt can migrate inwards, it could fall in the chaotic zone of the putative planet sculpting the outer belt, possibly continuing its inward migration and feeding the hot dust before being ejected or accreted. Assuming that the hot dust is fed by planet scattering in this manner, we can place constraints on the planet masses required, and thus, further constrain the orbital parameters of any interior planet. As the maximum kick a particle can experience when encountering a planet is of the order of the planet's escape velocity, v_{esc} , planets with v_{esc} much larger than the Keplerian velocity, v_{K} , will most likely eject particles after multiple kicks. On the other hand, if $v_{\text{esc}} \ll v_{\text{K}}$ then accretion will likely be the final outcome before the particle gets enough kicks to put it on an unbound orbit. As shown in

Wyatt et al. (2017), equating v_{esc} and v_K we can find roughly the planet mass that divides the two scenarios

$$M_{\text{plt}} = 40 \left(\frac{M_\star}{M_\odot} \right)^{3/2} \left(\frac{a_{\text{plt}}}{1 \text{ au}} \right)^{-3/2} \left(\frac{\rho_{\text{plt}}}{1 \text{ g cm}^{-3}} \right)^{-1/2} [M_\oplus], \quad (18)$$

where ρ_{plt} is the bulk mass of the planet, hereafter assumed to be 1.6 g cm^{-3} (Neptune's bulk density). This line is represented in Fig. 16 by a continuous black line. However, ejection might only happen after several encounters, thus, material can remain in the system for time-scales shorter than the ejection time-scale, which we take as the cometary diffusion time-scale derived empirically by Tremaine (1993). Using equation (2) from Wyatt et al. (2017) we find

$$M_{\text{plt}} = \left(\frac{M_\star}{M_\odot} \right)^{3/4} \left(\frac{a_{\text{plt}}}{1 \text{ au}} \right)^{3/4} \left(\frac{t_\star}{1 \text{ Gyr}} \right)^{-1} [M_\oplus]. \quad (19)$$

In Fig. 16, this is represented by a black-dashed line (using $t_\star = 1.4 \text{ Gyr}$). Therefore, particles encountering a planet with a mass above the one defined by equation (18) and below equation (19) will likely remain in the system without being ejected or accreted for time-scales longer than the age of the system. Thus, a planet that both truncated the disc (red and blue lines) and does not eject particles within 1.4 Gyr must have a mass $\lesssim 30 M_\oplus$. However, material formed farther out, e.g. in the outer belt, could fall in this region at late epochs and thus remain in the system until the present epoch even if the putative planet is more massive than $30 M_\oplus$.

Combining the four equations above we can define a region in M_{plt} versus a_{plt} space where the putative planet is most likely to be found. This is represented by a green region in Fig. 16, and roughly defined by a_{plt} in the range $\sim 75\text{--}100 \text{ au}$ and M_{plt} between 3 and $30 M_\oplus$. Planets in this region will have a semimajor axis such that they can truncate the disc by clearing their chaotic zone on a time-scale shorter than the age of the system. They will not force an eccentricity on the disc higher than 0.05, and they will not eject particles within 1.4 Gyr. Given the uncertainty on the age of the system (1–2 Gyr), the range of masses given above could change by 40 per cent. The mass upper limit is also consistent with the limits of a few Jupiter masses placed by direct imaging planet searches in this system.

Moreover, the planets in the green region have higher masses than the minimum mass to stir the outer belt on a time-scale equal to the age of the system. Assuming a forced eccentricity of 0.05, i.e. $e_{\text{plt}} \lesssim 0.08$, and using equation (15) from Mustill & Wyatt (2009) we find this mass is $1 M_\oplus$. Therefore, self-stirring is not necessary as a planet in this region would be able to stir the disc on a time-scale shorter than 1.4 Gyr.

4.1.5 Multiple planets

It is important to stress that our analysis above is only valid for a single planet. The planet truncating the disc could have a higher mass if other planets are present with smaller a_{plt} , such that particles initially scattered by the outermost planet get scattered inward by the inner planets before being ejected. In a chain of planets this can be achieved consecutively if each planet on the chain has a scattering time-scale shorter than the next planet with larger semimajor axis, such that particles get scattered faster by the inner planets, increasing the probability of migrating inwards. In other words, the scattering time-scale of the planets in the system has to increase with distance in order to maximize the inward torque. This could be

done by a flat distribution of planet mass with a_{plt} as the scattering time-scale scales with orbital period. However, a chain of planets with uniform mass above $30 M_\oplus$ would scatter material inwards until reaching the innermost planet which will eject particles in only a few encounters without feeding the hot dust.

Therefore, as discussed in Wyatt et al. (2017) we can hypothesize how a chain of planets should be distributed in mass and semimajor axis to maximize the influx from the outer to the inner most regions. The two basic requirements are: (1) the innermost planet within a few au should reside below the ejection region of Fig. 16, such that particles can remain in the inner regions for longer time-scales or produce giant impacts releasing large amounts of dusty debris as accretion is more likely; (2) the mass of planets should be close to a flat distribution or decrease with radius, maximizing the inward torque. Based on Fig. 16 and the two conditions above, we find that a chain of planets with uniform mass between 3 and $30 M_\oplus$ would satisfy the two conditions above, e.g. a chain of less than 10 planets separated by $\gtrsim 15$ mutual Hill radii with a mass of $\sim 10 M_\oplus$. Such a system would scatter particles from the outer regions until they encounter the innermost planet in the chain which would lie below the ejection region. Then, the hot dust excess observed in η Corvi could be the product of giant impacts releasing debris or the product of collisions between larger grains or planetesimals within a few au where collisions are more frequent and destructive.

4.1.6 The η Corvi sweet spot

In the scenario 3, the hot dust in η Corvi is the result of a giant collision of an embryo scattered from the outer disc with a planet at separations $\lesssim 3 \text{ au}$. Based on the work by Wyatt et al. (2017) we can place some constraint on this planet or others within a few au. In their work they estimated how long debris produced from a giant collision can remain at detectable levels before being accreted or collisionally depleted (see their equation 22 and fig. 5). In Fig. 16, we plot contours of the time-scales at which debris produced by a giant collision can remain above the current levels in η Corvi. We assumed that the giant impact puts in orbit a fraction $f_{\text{esc}} = 0.05$ of the mass of the planet, which evolves through mutual collision or it gets accreted by the planet. The debris is characterized by a maximum particle size of 100 km and a planetesimal threshold $Q_D^\star = 200 \text{ J kg}^{-1}$. SED modelling showed that the peak of the hot dust is around $20 \mu\text{m}$ with a fractional excess (R_{20}) of about 0.5 (Duchêne et al. 2014), thus we are interested in the time-scale at which the hot dust emission can stay above R_{20} , $t_{>R_\lambda}$. These time-scales are shown in Fig. 16 with yellow, orange and red contours.

From Fig. 16 we find that if giant collisions are uniformly likely in the $\log(a_{\text{plt}})\text{--}\log(M_{\text{plt}})$ space, an excess at $20 \mu\text{m}$ is more likely to be produced around 3–5 au by a collision on a planet of 4–10 M_\oplus . This excess would last around 10^4 years or a few thousands orbits. Throughout this time the debris would remain in an asymmetric distribution (Jackson et al. 2014). Such asymmetry would naturally explain why the emission is seen at a projected separation in the range 0.5–1 au by the LBTI (Defrère et al. 2015), but its temperature suggests a physical separation of $\sim 3 \text{ au}$ where the collision would have happened. Otherwise, this is hard to reconcile if the hot dust is produced in an axisymmetric disc, where a collisional cascade is fed from the outer belt (scenario 2). For scenario 2 to work this requires a very high albedo and a grain size distribution steeper than that expected from a collisional cascade (Lebreton et al. 2016), which thus means that scenario 3 may be favoured.

4.2 CO origin

Given the old age of η Corvi ($\gtrsim 1$ Gyr) any gas present in the system has to be of secondary origin, i.e. released from icy bodies present in the system. This could happen either in the outer belt or in the inner disc if CO is released as a consequence of collisions between icy bodies; however, the tentative detection of CO is not co-located with either of the two. Recently, Kral et al. (2016) studied the evolution of secondary gas in a debris disc when produced from a narrow ring. The gas can viscously spread forming an accretion disc, with a surface density that depends on the gas production rate and on the viscosity of the disc, expected to be higher than in a protoplanetary disc as the disc should be highly ionized (Kral & Latter 2016). Depending on the viscous time-scale and lifetime, different molecules or atomic species would have different distributions in the disc. For example, in the case of β Pic, CO gas is released at ~ 85 au from icy bodies and photodissociates in C+O, which then spread to form an atomic accretion disc. Atomic gas species such as H I, C I, C II and O I, products of the photodissociation of H₂O and CO can viscously spread in the disc before being accreted into the host star (Kral et al. 2016). On the other hand, CO has a photodissociation time-scale of ~ 300 yr (longer than 120 yr as it is slightly self-shielded; Matrà et al. 2017), which is only a fraction of an orbit, and then too short to be able to spread in the disc. This is why CO is found to be co-located with the millimetre-sized dust in the β Pic disc, where it is released (Dent et al. 2014; Matrà et al. 2017).

However, if gas is released closer in, e.g. at ~ 1 au where the hot dust is located in η Corvi, then CO could spread significantly outwards in the disc as both the orbital and viscous time-scales increase with radius. In order to assess if the CO could spread up to 20 au, we can estimate the viscous time-scale, t_v , for it assuming an α -parametrization for the viscosity (Shakura & Sunyaev 1973), i.e. $\nu = \alpha_v c_s H$, where c_s and H are the sound speed and the local disc scaleheight. Assuming $\alpha_v = 1.5$ (best-fitting model for β Pic; Kral et al. 2016) we find that $t_v \sim \frac{\Delta r^2}{\nu (r'_c)}$ is $\sim 10^4 - 10^5$ yr for $\Delta r = 20$ au and $r'_c = 1-20$ au. This is longer by at least two orders of magnitude than the photodissociation time-scale, and thus, CO would not be able to spread fast enough to reach 20 au before being photodissociated. If the CO production rate were high enough, CO could be self-shielded; however, the upper limit we found in Section 3.7 for a broad inner disc implies that the vertical column density of CO is $\lesssim 10^{14}$ cm⁻², not enough to be considerably self-shielded (Visser et al. 2009). Note that carbon ionization can also shield the CO, yet in β Pic this was found to be a minor effect compared to the CO self-shielding (Matrà et al. 2017). Assuming a carbon to CO abundance ratio of 100, carbon ionization would shield the CO only by a factor of 1.2, increasing its photodissociation time-scale to 140 yr (Rollins & Rawlings 2012). Another important issue with this scenario is that within a few au solids should be depleted of icy volatiles as the temperatures are significantly higher than 140 K, the maximum temperature at which CO or CO₂ can be trapped by amorphous H₂O ice (Collings et al. 2003). In η Corvi this temperature corresponds to the equilibrium temperature at 9 au. Therefore, icy material would have to pass very quickly this ice line to reach ~ 1 au to release the CO in destructive collisions of planetesimals or be large enough as the sublimation rate depends on their area, e.g. comets in Solar system that cross the water ice line can retain significant amounts of ices for several orbits.

Alternatively, the tentative CO detection at 22 ± 6 au could be explained by gas released *in situ*. Icy material formed in the outer belt and transported from cold regions should start to sublimate at a high rate when crossing a specific ice line or reaching spe-

cific temperatures. At 22 ± 6 au, the equilibrium temperature is 88 ± 12 K. Desorption experiments have studied in detail the desorption rate of volatiles in isolation or with the presence of water ice, as a function of the temperature. For example, in isolation the CO₂ desorption rate peaks at around 80 K (Collings et al. 2004), thus CO gas trapped in CO₂ ice could be released when crossing the CO₂ ice line; alternatively, as CO₂ photodissociates in about 30 yr into CO and O due to the interstellar UV radiation field (Hudson 1971; Lewis & Carver 1983), the observed CO could all come from CO₂ being photodissociated. For example, the coma activity of comet C/2012 S1 (ISON) on its last passage was likely controlled by CO₂ ice sublimation beyond the water ice line (Meech et al. 2013). Another possibility is that if the volatile content in planetesimals is dominated by water ice, the desorption rates of other molecules can be modified as they get trapped by amorphous water ice. This is true for trapped CO and CO₂ reaching a maximum desorption rate at ~ 140 K during water crystallization and at 160 K when water starts to sublimate, allowing trapped volatiles to desorb (Collings et al. 2003, 2004). In fact, this is observed in Solar system comets, where the composition of their coma changes from CO- to H₂O-driven near 2.5 au, where the comet surface temperatures reach ~ 150 K (e.g. Comet Hale-Bopp (C/1995 O1) and others, Biver et al. 1997; Ootsubo et al. 2012). Therefore, CO could be released *in situ* explaining the tentative detection without the need of being released in collisions and viscously expand from close in regions where the hot dust is. It is also worth noting that the location at which these temperatures are reached depend also on the surface physical properties of the icy material, e.g. if it is covered by ice or dust, on the rotation rates and if volatiles are being released from small grains or not, and they can even vary significantly across the surface of big comets (Choukroun et al. 2015, e.g. comet 67P/Churyumov-Gerasimenko.). Numerical simulations by Marboeuf, Bonsor & Augereau (2016) have explored the thermo-physical evolution of comets and production rates of H₂O gas and dust from their surface, finding for example that the H₂O gas and dust production rates increase exponentially from tens of au down to 6 au for $L_* = 5 L_\odot$. Therefore, the CO location and radial distribution, together with thermo-physical models of comets including other molecule species such as CO and CO₂, can give clues about the nature of these exocomets and composition.

The latter scenario fits with the hypothesis of icy material being passed from the outer belt to the inner regions. The non-detection of CO closer in could be explained if the icy material gets depleted of volatiles before reaching the inner regions where the hot dust is. This would imply that the time-scale at which material loses its volatile content is shorter than the time-scale at which material migrates from ~ 20 to ~ 10 au, i.e. $\lesssim 2 \times 10^4$ yr (using the lower limit on the migration rate for a surface density of solids proportional to r^{-1} derived in Section 4.1.2). Alternatively, the non-detection could be also explained by the CO lifetime getting shorter for smaller radii as the UV stellar radiation starts to dominate in the photodissociation process, reducing the amount of CO gas. Moreover, we find that the CO destruction rate, which is $\sim 3 \times 10^{-9} M_\oplus \text{ yr}^{-1}$, is of the same order as the hot dust mass-loss rate. This implies that the material from the outer belt passed in is highly rich in CO or CO₂ (~ 50 per cent of mass in CO) or that only a fraction of the material that reaches 20 au continues its way in to collide where the hot dust is.

One potential problem with this scenario is that if the CO present in the disc is produced in steady state, i.e. constantly released at a rate of $\sim 3 \times 10^{-9} M_\oplus \text{ yr}^{-1}$, it would imply that over a time-scale of 1.4 Gyr the outer belt has lost $\sim 4 M_\oplus$ of CO or $40 M_\oplus$ in

planetesimals assuming a CO mass fraction of 10 per cent in solids (value consistent with Solar system comets; Mumma & Charnley 2011). This value is of the order of the total amount of solids initially present at the outer belt location if we extrapolate the minimum mass solar nebula (Weidenschilling 1977) surface density profile ($30 M_{\oplus}$), and similar to the initial Kuiper belt mass in the Nice model ($35 M_{\oplus}$; Gomes et al. 2005). However, this assumes that the amount of CO gas present at 20 au is in steady state, which is not necessarily the case. For example, if the hot dust is fed by particles with a wide size distribution, small grains would be fed continuously, whereas bigger particles which contain most of the mass would behave stochastically as the number is much lower. Therefore, we could be witnessing a rare event in this system. This is similar to the stochastic accretion proposed to explain the pollution on white dwarfs (Wyatt et al. 2014). If the tentative CO detection is confirmed and its distribution resolved, it would help to constrain better how the hot dust is being fed from material originated in the outer belt.

5 CONCLUSIONS

In this paper, we have presented the first ALMA observations of the debris disc around η Corvi at 0.88 mm, obtaining the most detailed image of its outer belt up to date. We detected the outer disc at all azimuths, with a peak radius of 150 au and radially spanning over 70 au or more, consistent with being axisymmetric and with previous observations.

In order to obtain estimates of different disc parameters with uncertainties, we model the emission using a number of four-disc models and compared them with the observed visibilities. The first model consists of a simple belt with radial and vertical Gaussian mass distributions. We found the outer belt density distribution peaks at 150 ± 3 au, with a radial FWHM of 44 ± 6 au. This model gives the best fit to the observations with a total flux of 13 ± 1 mJy. The second model consists of the expected profile from a self-stirred disc. We found that the derived disc parameters in the self-stirred scenario imply an unphysically high range of surface density of solids in the primordial disc. However, self-stirring could still be the case if the outer belt was initially narrow or truncated by a planet.

Because of the comet-like composition of the hot dust and its short lifetime, it has been suggested that it is being fed from the outer belt. Several mechanisms could be responsible for such delivery. Previous observations ruled out all except three, one of which proposes that the system is going through LHB-like instability. We compared simulated observations using as input one of the LHB models, scaled to the size of the η Corvi outer belt, finding that the surface density radial profile from LHB simulations is too broad compared to the η Corvi outer belt. Moreover, a double power-law fit to the disc surface density indicates that it must increase steeply from the inner regions to the outer belt, in contradiction with a highly scattered belt produced after an instability. We also fit an eccentric disc model, finding that the disc is consistent with being circular and with a 3σ upper limit for the belt eccentricity of 0.05. Therefore, we conclude that the outer belt is probably in a stable configuration on Gyr time-scales, where a chain of planets is scattering in material from the outer belt.

Although the exact mechanism or planetary configuration scattering material inwards is unknown, we placed upper limits on any millimetre extended emission from dust inside the cavity based on the measured visibilities. These limits can be used in the future to place constraints on the distribution of solids if solid material is in-

deed being transported from the outer belt to the inner most regions of the system.

We searched for any CO gas that could be present in the disc. Although we did not detect gas in the outer belt or co-located with the hot dust, we present a tentative detection of CO gas around ~ 20 au. Considering non-LTE effects, we derived a CO gas mass estimate based on a tentative CO detection at ~ 20 au and 3σ upper limits according to the non-detections in the outer belt and inner regions. Regarding the origin of the putative CO gas, we find that it could be released *in situ* from icy bodies when crossing an ice line, e.g. CO₂ sublimates at ~ 80 K, which could then release trapped CO or produce it via photodissociation. Alternatively, CO gas trapped in porous H₂O ice could be released following the crystallization of water or its sublimation when reaching 140 or 150 K, respectively. The latter scenario is consistent with the hypothesis that material being transported from the outer belt to the location of the hot dust and suggests that we could be observing the system with a particularly high activity after a recent event. It is unlikely that the observed CO gas is being produced within a few au and viscously expanding outwards up to 20 au, as time-scales for photodissociation are shorter than viscous evolution.

Finally, based on these new observations and the estimates of the inner edge of the disc and disc eccentricity we put some constraints on any planet that is responsible for truncating the disc at ~ 106 au in a time-scale shorter than the age of the system, inducing a forced eccentricity lower than 0.05, and with a mass and semi-major axis such that it scatters material from the outer disc that can move inwards without being ejected from the system on time-scales of the order of the age of the system. Under these restrictions, we find that such planet should have a semimajor axis around 75–100 au, a mass between 3 and $30 M_{\oplus}$ and an eccentricity lower than 0.08.

Therefore, we proposed the following global scenario: volatile-rich solid material formed in the outer belt is being passed in via scattering with a chain of planets in the system. This icy material starts to sublimate and loses part of its volatiles when crossing specific ice line(s), explaining the CO at ~ 20 au. The chain of planets should have a mass distribution close to flat between 3 and $30 M_{\oplus}$ to maximize the mass flux into the inner regions where the hot dust lies. Finally, the inflowing material feeds an *in situ* collisional cascade or collides with a planet with a mass of 4–10 M_{\oplus} located at ~ 3 au (sweet spot of the system) releasing large amounts of debris and resulting in an asymmetric structure, consistent with LBTI observations and the observed spectroscopic features. This can be tested by (1) confirming the CO detection and resolving in both radius and azimuth the distribution of gas in the disc with deeper ALMA observations; (2) detecting any extended dust emission inside the cavity combining ALMA and ACA or with SMA observations reaching a higher sensitivity on large scales; (3) follow up LBTI observations to constrain the hot dust distribution which should remain constant and asymmetric in a giant impact scenario; (4) RV upper limits of planets that discard the presence of an ejector within 3 au ($\gtrsim 0.1 M_{\text{Jup}}$); (5) direct imaging to search for outer planets, which at $10 M_{\oplus}$ would be challenging to detect directly, but could have an enhanced brightness if surrounded by dust (Kennedy & Wyatt 2011); (6) *N*-body simulations tailored to the system.

ACKNOWLEDGEMENTS

We thank Pablo Roman and Simon Casassus for providing us the tool `UVSIM` to simulate model visibilities. This paper makes use of the following ALMA data: ADS/JAO.ALMA 2012.1.00385.S.

ALMA is a partnership of ESO (representing its member states), NSF (USA) and NINS (Japan), together with NRC (Canada) and NSC and ASIAA (Taiwan) and KASI (Republic of Korea), in cooperation with the Republic of Chile. The Joint ALMA Observatory is operated by ESO, AUI/NRAO and NAOJ. MCW, LM, AB and QK acknowledge the support of the European Union through ERC grant number 279973. LM also acknowledges support by STFC through a graduate studentship. The work of OP is supported by the Royal Society Dorothy Hodgkin Fellowship. GMK is supported by the Royal Society as a Royal Society University Research Fellow.

REFERENCES

- Absil O. et al., 2013, *A&A*, 555, A104
- Backman D. E., Paresce F., 1993, in Levy E. H., Lunine J. I. ed., *Protostars and Planets III* (A93-42937 17-90), p. 1253
- Biver N. et al., 1997, *Science*, 275, 1915
- Bohren C. F., Huffman D., 1983, *Absorption and Scattering of Light by Small Particles*. Wiley, New York, Wiley Science Paperback Series. Available at: <http://books.google.cl/books?id=S1RCZ8BjgNOC>
- Bonsor A., Wyatt M. C., 2012, *MNRAS*, 420, 2990
- Bonsor A., Augereau J.-C., Thébault P., 2012, *A&A*, 548, A104
- Bonsor A., Raymond S. N., Augereau J.-C., 2013, *MNRAS*, 433, 2938
- Bonsor A., Raymond S. N., Augereau J.-C., Ormel C. W., 2014, *MNRAS*, 441, 2380
- Booth M., Wyatt M. C., Morbidelli A., Moro-Martín A., Levison H. F., 2009, *MNRAS*, 399, 385
- Borgniet S., Lagrange A.-M., Meunier N., Galland F., 2016, preprint ([arXiv:1608.08257](https://arxiv.org/abs/1608.08257))
- Brown M. E., 2002, *Annu. Rev. Earth Planet. Sci.*, 30, 307
- Carpenter J. M. et al., 2009, *ApJS*, 181, 197
- Casagrande L., Schönrich R., Asplund M., Cassisi S., Ramírez I., Meléndez J., Bensby T., Feltzing S., 2011, *A&A*, 530, A138
- Casassus S., Perez M. S., Jordán A., Ménard F., Cuadra J., Schreiber M. R., Hales A. S., Ercolano B., 2012, *ApJ*, 754, L31
- Casassus S. et al., 2013, *Nature*, 493, 191
- Casassus S. et al., 2015, *ApJ*, 811, 92
- Cataldi G. et al., 2014, *A&A*, 563, A66
- Chen C. H. et al., 2006, *ApJS*, 166, 351
- Choukroun M. et al., 2015, *A&A*, 583, A28
- Collings M. P., Dever J. W., Fraser H. J., McCoustra M. R. S., Williams D. A., 2003, *ApJ*, 583, 1058
- Collings M. P., Anderson M. A., Chen R., Dever J. W., Viti S., Williams D. A., McCoustra M. R. S., 2004, *MNRAS*, 354, 1133
- Defrère D. et al., 2015, *ApJ*, 799, 42
- Dent W. R. F. et al., 2014, *Science*, 343, 1490
- Draine B. T., 2003, *ApJ*, 598, 1017
- Duchêne G. et al., 2014, *ApJ*, 784, 148
- Dullemond C., Juhasz A., Pohl A., Sereshti F., Shetty R., Peters T., Commerçon B., Flock M., 2015, *RADMC3D v0.39* <http://www.ita.uni-heidelberg.de/dullemond/software/radmc-3d/>
- Eiroa C. et al., 2013, *A&A*, 555, A11
- Españillat C. et al., 2014, *Protostars and Planets VI*. University of Arizona Press, Tucson, p. 497
- Fontenla J. M., Balasubramaniam K. S., Harder J., 2007, *ApJ*, 667, 1243
- Foreman-Mackey D., Hogg D. W., Lang D., Goodman J., 2013, *PASP*, 125, 306
- Foreman-Mackey D., Price-Whelan A., Ryan G., Emily Smith M., Barbary K., Hogg D. W., Brewer B. J., 2014, preprint, [triangle.py v0.1.1](https://arxiv.org/abs/1405.2811), doi: 10.5281/zenodo.11020,
- Fukagawa M., Tamura M., Itoh Y., Kudo T., Imaeda Y., Oasa Y., Hayashi S. S., Hayashi M., 2006, *ApJ*, 636, L153
- Gomes R., Levison H. F., Tsiganis K., Morbidelli A., 2005, *Nature*, 435, 466
- Gontcharov G. A., 2006, *Astron. Lett.*, 32, 759
- Goodman J., Weare J., 2010, *Commun. Appl. Math. Comput. Sci.*, 5, 65
- Hillenbrand L. A. et al., 2008, *ApJ*, 677, 630
- Hudson R. D., 1971, *Rev. Geophys. Space Phys.*, 9, 305
- Ibukiyama A., Arimoto N., 2002, *A&A*, 394, 927
- Jackson A. P., Wyatt M. C., Bonsor A., Veras D., 2014, *MNRAS*, 440, 3757
- Kass R. E., Raftery A. E., 1995, *J. Am. Stat. Assoc.*, 90, 773
- Kennedy G. M., Piette A., 2015, *MNRAS*, 449, 2304
- Kennedy G. M., Wyatt M. C., 2010, *MNRAS*, 405, 1253
- Kennedy G. M., Wyatt M. C., 2011, *MNRAS*, 412, 2137
- Kennedy G. M., Wyatt M. C., 2013, *MNRAS*, 433, 2334
- Kennedy G. M., Wyatt M. C., 2014, *MNRAS*, 444, 3164
- Kennedy G. M., Wyatt M. C., Sibthorpe B., Phillips N. M., Matthews B. C., Greaves J. S., 2012, *MNRAS*, 426, 2115
- Kennedy G. M. et al., 2015, *ApJS*, 216, 23
- Kenyon S. J., Bromley B. C., 2008, *ApJS*, 179, 451
- Kral Q., Latter H., 2016, *MNRAS*, 461, 1614
- Kral Q., Thébault P., Augereau J.-C., Boccaletti A., Charnoz S., 2015, *A&A*, 573, A39
- Kral Q., Wyatt M., Carswell R. F., Pringle J. E., Matrà L., Juhász A., 2016, *MNRAS*, 461, 845
- Kurucz R. L., 1979, *ApJS*, 40, 1
- Lacour S. et al., 2016, *A&A*, 590, A90
- Lagrange A.-M., Desort M., Galland F., Udry S., Mayor M., 2009, *A&A*, 495, 335
- Lebreton J., Beichman C., Bryden G., Defrère D., Mennesson B., Millan-Gabet R., Boccaletti A., 2016, *ApJ*, 817, 165
- Lewis B. R., Carver J. H., 1983, *J. Quant. Spec. Radiat. Transf.*, 30, 297
- Li A., Greenberg J. M., 1997, *A&A*, 323, 566
- Li A., Greenberg J. M., 1998, *A&A*, 331, 291
- Lissauer J. J., 1987, *Icarus*, 69, 249
- Lissauer J. J., 1993, *ARA&A*, 31, 129
- Lisse C. M., Chen C. H., Wyatt M. C., Morlok A., Song I., Bryden G., Sheehan P., 2009, *ApJ*, 701, 2019
- Lisse C. M. et al., 2012, *ApJ*, 747, 93
- Löhne T., Krivov A. V., Rodmann J., 2008, *ApJ*, 673, 1123
- Loukitcheva M., Solanki S. K., Carlsson M., Stein R. F., 2004, *A&A*, 419, 747
- McMullin J. P., Waters B., Schiebel D., Young W., Golap K., 2007, in Shaw R. A., Hill F., Bell D. J., eds, *ASP Conf. Ser. Vol. 376, Astronomical Data Analysis Software and Systems XVI*. Astron. Soc. Pac., San Francisco, p. 127
- Mallik S. V., Parthasarathy M., Pati A. K., 2003, *A&A*, 409, 251
- Marboeuf U., Bonsor A., Augereau J.-C., 2016, preprint ([arXiv:1604.03790](https://arxiv.org/abs/1604.03790))
- Marino S. et al., 2016, *MNRAS*, 460, 2933
- Matrà L., Panić O., Wyatt M. C., Dent W. R. F., 2015, *MNRAS*, 447, 3936
- Matrà L. et al., 2017, *MNRAS*, 464, 1415
- Matthews B. C., Krivov A. V., Wyatt M. C., Bryden G., Eiroa C., 2014, in Beuther H., Klessen R. S., Dullemond C. P., Henning T., eds, *Protostars and Planets VI*, Univ. Arizona Press, Tucson, p. 521
- Meech K. J. et al., 2013, *ApJ*, 776, L20
- Mumma M. J., Charnley S. B., 2011, *ARA&A*, 49, 471
- Mustill A. J., Wyatt M. C., 2009, *MNRAS*, 399, 1403
- Mustill A. J., Wyatt M. C., 2012, *MNRAS*, 419, 3074
- Ootsubo T. et al., 2012, *ApJ*, 752, 15
- Pan M., Nesvold E. R., Kuchner M. J., 2016, preprint ([arXiv:1607.06798](https://arxiv.org/abs/1607.06798))
- Pearce T. D., Wyatt M. C., 2014, *MNRAS*, 443, 2541
- Pinilla P., Benisty M., Birnstiel T., 2012, *A&A*, 545, A81
- Roberge A., Feldman P. D., Lagrange A. M., Vidal-Madjar A., Ferlet R., Jolly A., Lemaire J. L., Rostas F., 2000, *ApJ*, 538, 904
- Rollins R. P., Rawlings J. M. C., 2012, *MNRAS*, 427, 2328
- Schwarz G., 1978, *Ann. Stat.*, 6, 461
- Shakura N. I., Sunyaev R. A., 1973, *A&A*, 24, 337
- Shannon A., Bonsor A., Kral Q., Matthews E., 2016, *MNRAS*, 462, L116
- Smith R., Wyatt M. C., Haniff C. A., 2009, *A&A*, 503, 265
- Stencel R. E., Backman D. E., 1991, *ApJS*, 75, 905
- Su K. Y. L. et al., 2006, *ApJ*, 653, 675

- Sylvester R. J., Skinner C. J., Barlow M. J., Mannings V., 1996, MNRAS, 279, 915
- Thureau N. D. et al., 2014, MNRAS, 445, 2558
- Toomre A., 1964, ApJ, 139, 1217
- Tremaine S., 1993, in Phillips J. A., Thorsett S. E., Kulkarni S. R., eds, ASP Conf. Ser. Vol. 36, Planets Around Pulsars. Astron. Soc. Pac., San Francisco, p. 335
- van Leeuwen F., 2007, A&A, 474, 653
- Verhoeff A. P. et al., 2011, A&A, 528, A91
- Vican L., 2012, AJ, 143, 135
- Visser R., van Dishoeck E. F., Black J. H., 2009, A&A, 503, 323
- Weidenschilling S. J., 1977, MNRAS, 180, 57
- Wisdom J., 1980, AJ, 85, 1122
- Wyatt M. C., 2008, ARA&A, 46, 339
- Wyatt M. C., Greaves J. S., Dent W. R. F., Coulson I. M., 2005, ApJ, 620, 492
- Wyatt M. C., Smith R., Greaves J. S., Beichman C. A., Bryden G., Lisse C. M., 2007a, ApJ, 658, 569
- Wyatt M. C., Smith R., Su K. Y. L., Rieke G. H., Greaves J. S., Beichman C. A., Bryden G., 2007b, ApJ, 663, 365
- Wyatt M. C., Booth M., Payne M. J., Churcher L. J., 2010, MNRAS, 402, 657
- Wyatt M. C., Farihi J., Pringle J. E., Bonsor A., 2014, MNRAS, 439, 3371
- Wyatt M. C., Bonsor A., Jackson A. P., Marino S., Shannon A., 2017, MNRAS, 464, 3385

This paper has been typeset from a $\text{\TeX}/\text{\LaTeX}$ file prepared by the author.